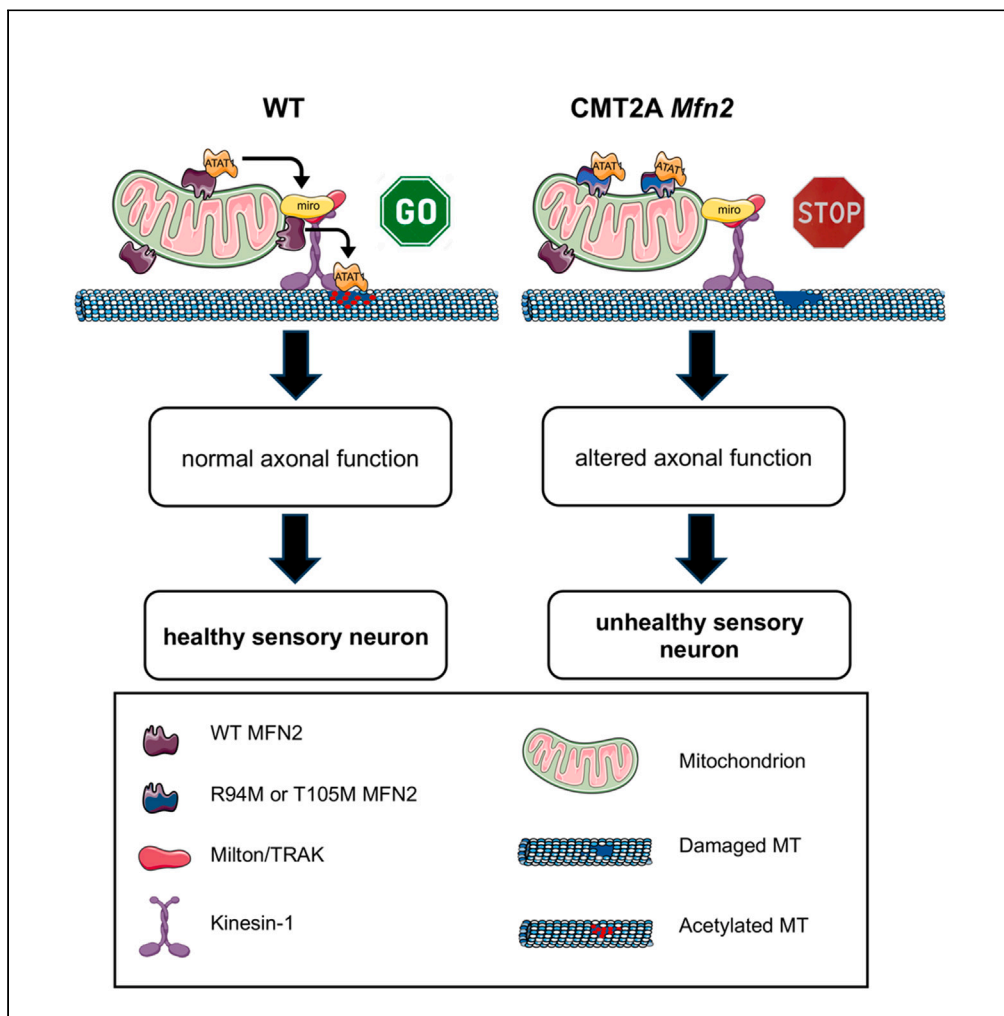**Article**

MFN2 coordinates mitochondria motility with α-tubulin acetylation and this regulation is disrupted in CMT2A

Atul Kumar,
Delfina Larrea,
Maria Elena Pero,
..., Lucia Di
Marcotullio, Estela
Area-Gomez,
Francesca Bartolini

fb2131@columbia.edu

Highlights

Mitochondria-MT contacts
are hotspots for MFN2/
ATAT1-mediated tubulin
acetylation

Mutations in MFN2
associated with CMT2A
alter MNF2/ATAT1
binding

Axonal degeneration by
loss of MFN2 depends on
decreased acetylated
tubulin

Article

MFN2 coordinates mitochondria motility with α-tubulin acetylation and this regulation is disrupted in CMT2A

Atul Kumar,[1] Delfina Larrea,[2] Maria Elena Pero,[1,3] Paola Infante,[4] Marilisa Conenna,[1,4] Grace J. Shin,[5,9,10,11] Vincent Van Elias,[1] Wesley B. Grueber,[5,6] Lucia Di Marcotullio,[4,7] Estela Area-Gomez,[2,8] and Francesca Bartolini[1,12,*]

SUMMARY

Mitofusin-2 (MFN2), a large GTPase residing in the mitochondrial outer membrane and mutated in Charcot-Marie-Tooth type 2 disease (CMT2A), is a regulator of mitochondrial fusion and tethering with the ER. The role of MFN2 in mitochondrial transport has however remained elusive. Like MFN2, acetylated microtubules play key roles in mitochondria dynamics. Nevertheless, it is unknown if the α-tubulin acetylation cycle functionally interacts with MFN2. Here, we show that mitochondrial contacts with microtubules are sites of α-tubulin acetylation, which occurs through MFN2-mediated recruitment of α-tubulin acetyltransferase 1 (ATAT1). This activity is critical for MFN2-dependent regulation of mitochondria transport, and axonal degeneration caused by CMT2A MFN2 associated R94W and T105M mutations may depend on the inability to release ATAT1 at sites of mitochondrial contacts with microtubules. Our findings reveal a function for mitochondria in α-tubulin acetylation and suggest that disruption of this activity plays a role in the onset of MFN2-dependent CMT2A.

INTRODUCTION

Charcot-Marie-Tooth type 2A (CMT2A) disease is a predominantly axonal form of familial peripheral neuropathy causing sensory loss that results from degeneration of long peripheral axons.[1] Inherited dominant mutations in the mitochondrial fusion protein mitofusin-2 (MFN2), a large GTPase residing in the outer mitochondrial membrane (OMM) and endoplasmic reticulum (ER), are the most common causes of CMT2A. The majority of MFN2 mutations affect the amino terminal GTPase domain, with disease onset in the first two years of life and an aggressive clinical course.[2,3] MFN2 plays crucial roles in mitochondria dynamics, including regulation of fusion, motility, and ER/mitochondria contacts.[4] Defects in mitochondria dynamics are typically associated with CMT pathogenesis, including CMT caused by MFN2 mutations.[5–8] However, the mechanisms by which mutant MFN2 contributes to CMT2A remain elusive.

Together with mitofusin-1 (MFN1), MFN2 regulates mitochondrial fusion, which is essential to maintain proper mitochondrial distribution, shape and degradation.[4] In addition, MFN2 plays a role in ER-mitochondrial tethering that is independent of its fusion function, by bonding mitochondria with mitochondria-associated ER membranes (MAMs) to provide ATP, Ca^{2+} and lipid transfer.[5,9–12] Accordingly, MFN2 regulates the rate of cholesterol esterification, which was proposed to be a proxy of MAM function, and the extent of contact points between the ER and mitochondria.[13]

A fusion and tethering independent role for MFN2 in regulating mitochondrial axonal transport has been reported. Loss of MFN2 or MFN2 disease mutants selectively alter mitochondrial axonal motility and distribution.[6,14,15] In addition, MFN2 deficiency in human spinal motor neurons interferes with mitochondrial transport while reducing the expression of kinesin and dynein motors,[16] which may further contribute to impaired mitochondrial motility. Importantly, both MFN1 and MFN2 interact with mammalian miro (miro1/miro2) and milton/TRAK (OIP106/GRIF1) proteins, members of the molecular machinery that links mitochondria to kinesin motors,[14] and overexpression of MFN1

[1]Department of Pathology & Cell Biology, Columbia University Irving Medical Center, New York, NY 10032, USA
[2]Department of Neurology, Columbia University Irving Medical Center, New York, NY 10032, USA
[3]Department of Veterinary Medicine and Animal Production, University of Naples Federico II, 80137 Naples, Italy
[4]Department of Molecular Medicine, University of Rome "La Sapienza", 00161 Rome, Italy
[5]Department of Neuroscience, Zuckerman Mind Brain Behavior Institute, Columbia University, New York, NY 10027, USA
[6]Department of Physiology & Cellular Biophysics, Zuckerman Mind Brain Behavior Institute, Columbia University, New York, NY 10032, USA
[7]Istituto Pasteur-Fondazione Cenci Bolognetti, University of Rome La Sapienza, Rome, Italy
[8]Present address: Department de Biología Celular y Molecular, Centro de Investigaciones Biológicas, MARGARITA SALAS, CSIC, 28040 Madrid, Spain
[9]Present address: Department of Neurology, The Ohio State University Wexner Medical Center, Columbus, OH, USA
[10]Present address: The Neuroscience Research Institute, The Ohio State University, Columbus, OH, USA
[11]Present address: The Ohio State University Comprehensive Cancer Center, Columbus, OH, USA
[12]Lead contact
*Correspondence: fb2131@columbia.edu
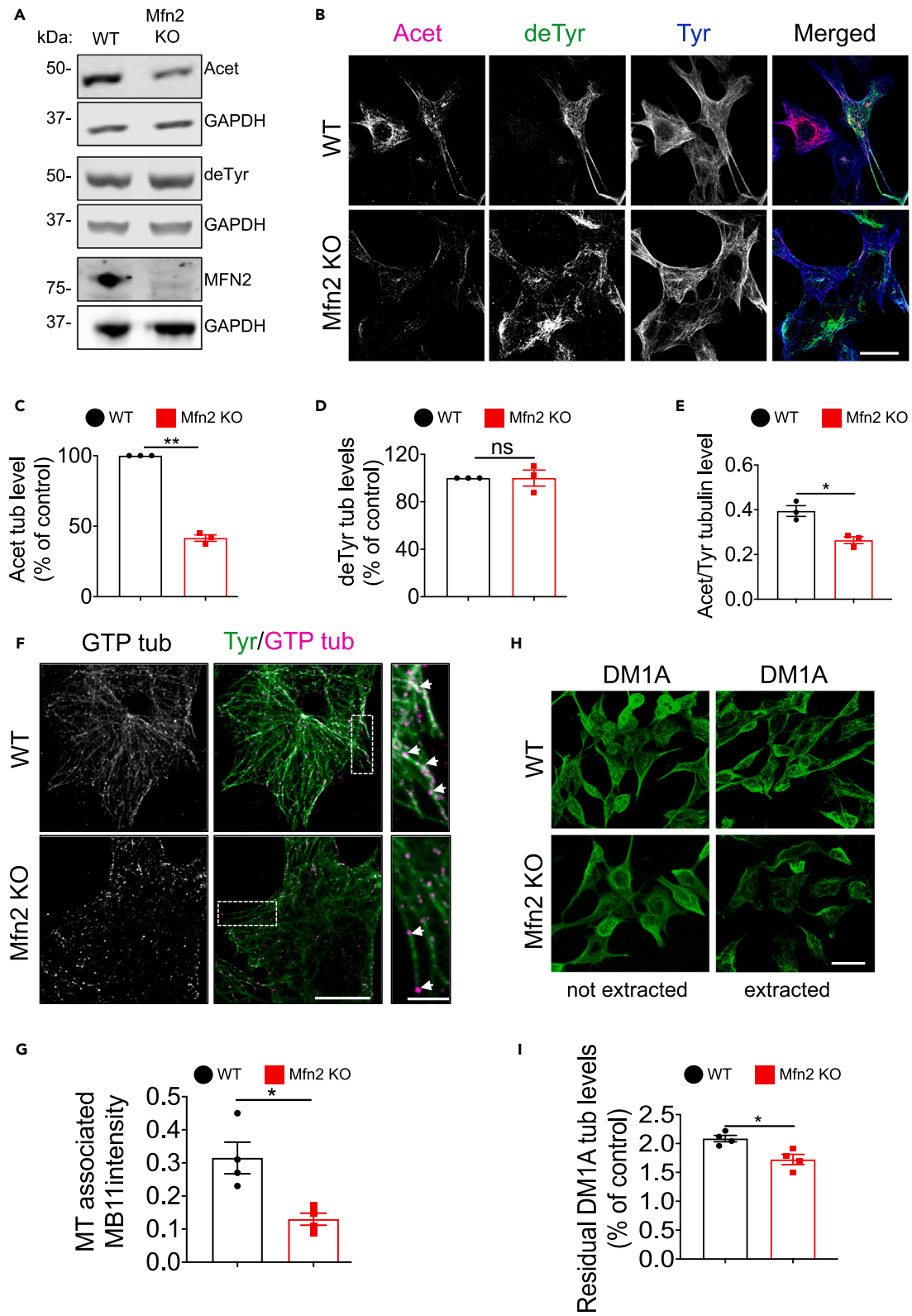https://doi.org/10.1016/j.isci.2024.109994

Figure 1. MFN2 regulates α-tubulin acetylation, MT dynamics and MT stability in MEFs

(A) Representative immunoblot of WT and Mfn2 KO whole MEF lysates. Acet, acetylated tubulin; deTyr, detyrosinated tubulin; Mfn2, mitofusin 2; GAPDH, loading control.

(B) Representative confocal immunofluorescence images (max projections from z-stacks) of WT and Mfn2 KO MEFs. Tyr, tyrosinated tubulin; Acet, acetylated tubulin; Tyr, tyrosinated tubulin. Scale bars, 10 μm.

(C and D) (C) Quantification of acetylated (Acet) and (D) detyrosinated (deTyr) tubulin immunofluorescence signal intensity normalized to WT control levels (N = 150–175 cells).

(E) Quantification of acetylated (Acet) to tyrosinated (Tyr) tubulin immunofluorescence signal intensity ratio in WT and Mfn2 KO MEFs.

(F) Representative confocal immunofluorescence images (max projections from z-stacks) GTP tubulin staining in WT and Mfn2 KO MEFs using hMB11 antibody staining. Scale bar, 10 μm; 5 μm (zoom image).

(G) Quantification of GTP-tubulin (MB11) immunofluorescence signal intensity associated with MTs in WT and Mfn2 KO MEFs (N = 20–25 cells).

(H) Representative confocal immunofluorescence images (max projection) of residual MT staining (DM1A) in WT and Mfn2 KO extracted MEFs. Scale bar, 10 μm.

(I) Quantification of residual DM1A tubulin levels in WT and Mfn2 KO MEFs treated as in H (N = 100–125 cells). Data are expressed as median with interquartile range. n = 3 independent experiments *p < 0.05; **p < 0.01; ns non-significant by Mann–Whitney U test.

rescues the axonal degeneration caused by MFN2 mutants *in vitro* and *in vivo*.[15,17] Altogether, these data support the notion that MFN2 may directly influence mitochondrial positioning, and that loss of this function in CMT contributes to the degeneration of long axons, which are particularly sensitive to failures in meeting local energy and calcium buffering demands. This model is consistent with the observation that most of the genes mutated in predominantly axonal forms of CMT have roles in mitochondrial motility, suggesting that impaired mitochondrial transport may be a common mechanism of CMT pathogenesis.[7] Despite this compelling evidence, the molecular basis underlying MFN2-dependent regulation of mitochondria positioning remains poorly understood. Furthermore, while loss of MFN2 induces neuropathy, the detailed mechanisms by which MFN2 deficiency results in axonal degeneration are unknown.

In sensory neurons, acetylated tubulin is an essential component of the mammalian mechanotransduction machinery due to its regulation of cellular stiffness and transient receptor potential (TRP) channel activity.[18–20] Importantly, loss of acetylated tubulin is a neuropathological feature of vincristine-induced toxicity[21] and mutant MFN2 (MFN2 R94Q)-mediated neuropathy in mice.[22] Acetylation of lys-40 in α-tubulin is predominantly regulated by tubulin N-acetyltransferase 1 (αTAT1 or ATAT1) and histone deacetylase 6 (HDAC6), two soluble enzymes that catalyze the forward and backward reaction, respectively.[23–26] Notably, enhancing tubulin acetylation by HDAC6 inhibitors has been largely successful in restoring axonal integrity and myelination of toxic and genetically inherited forms of peripheral neuropathy, including CMT.[21,22,27] Given the multitude of HDAC6 substrates in addition to tubulins, however, the mechanisms underlying this rescue remain unclear.

Tubulin acetylation on lys-40 is an α-tubulin PTM marking the luminal surface of MTs,[28,29] a unique feature that helps the MT lattice cope with mechanical stress via reduced lateral interactions between protofilaments[30] while facilitating MT self-repair through incorporation of GTP-bound tubulin subunits.[31,32] It is perhaps thanks to these MT features that mitochondria fusion, fission and ER/mitochondria contacts occur selectively on acetylated MTs[33,34] and that like MFN2, acetylated microtubules (MTs) play key roles in mitochondria dynamics. It is however unknown if the α-tubulin acetylation cycle can functionally interact with MFN2. In this study, we find that mitochondria contacts with MTs are hotspots of tubulin acetylation through the recruitment of ATAT1 by MFN2 onto mitochondrial outer membranes and that this activity is altered by MFN2 R94W and T105M CMT2A mutations. Furthermore, we provide evidence that axonal degeneration caused by MFN2 loss of function in dorsal root ganglion (DRG) neurons depends on loss of acetylated tubulin by disrupting mitochondria motility rather than mitochondrial fusion or tethering with the ER.

RESULTS

MFN2 is a regulator of α-tubulin acetylation

Despite the intimate relationship between acetylated MTs and mitochondria dynamics, it is unknown if the machinery controlling mitochondria motility and/or hetero-homotypic mitochondrial contacts functionally interacts with the α-tubulin acetylation cycle. To test this hypothesis, we measured levels of acetylated α-tubulin in immortalized Mfn2 KO mouse embryonic fibroblast (MEF) cells with reported defects in mitochondria dynamics and functional tethering with the ER.[35] By immunoblot and immunofluorescence analyses, we found that while detyrosinated tubulin levels were unaffected, loss of MFN2 reduced acetylated tubulin by more than 50% compared to WT controls (Figures 1A–1E and S1A–S1D). Loss of acetylated tubulin in these cells also correlated with a decrease in the abundance of GTP-tubulin islands, the putative entry sites for the tubulin acetyltransferase ATAT1 into the MT lumen and hotspots of MT self-repair by incorporation of GTP-bound tubulin subunits[36–39] (Figures 1F and 1G).

We measured MT plus end dynamics by following the behavior of individual MTs in WT and Mfn2 KO cells transfected with GFP-tubulin and found that lack of MFN2 expression almost doubled MT dynamicity, an effect due to an increase in MT growth and shrinkage rates (Table 1). The rise in MT dynamicity correlated with a significant loss of MT stability. To test this, we measured the amount of residual MT polymer resisting depolymerization that was induced by mild detergent extraction prior to fixation and immunofluorescence staining (Figures 1H and 1I). Importantly, both acetylated tubulin levels and MT dynamics were normalized in Mfn2 KO cells by the HDAC class I/II inhibitor trichostatin A (TSA) (Figures S1A–S1D and Table S1), suggesting that the increase in MT dynamicity resulted from loss of α-tubulin acetylation in cells deprived of MFN2.

Table 1. MFN2 regulates MT dynamics in MEFs

	WT	Mfn2 KO
Growth rate (μm/s)	0.05 ± 0.02	0.13 ± 0.006[a]
Shrinkage rate (μm/s)	0.07 ± 0.004	0.12 ± 0.01[a]
Catastrophe freq. (s-1)	0.06 ± 0.006	0.06 ± 0.004
Rescue freq. (s-1)	0.08 ± 0.006	0.08 ± 0.006
% Growth	35.5 ± 1.92	44.15 ± 0.95[b]
% Shrinkage	34.05 ± 0.87	36.48 ± 1.27[a]
% Pause	29.58 ± 0.62	20.1 ± 1.45
MT lifetime (s)	58.25 ± 2.14	60.5 ± 1.73
MT dynamicity (μm/min)	5.96 ± 0.42	10.43 ± 0.25[b]
Number of MTs	20	20

MT dynamics were measured from time-lapse analysis of GFP-tubulin-labeled MTs using epifluorescence microscopy (1f/5s). Parameters characterizing MT dynamics, such as the growth rate, the shrinkage rate, the frequency of 'catastrophe' (transitions from growth/pause to shortening) and 'rescue' (transitions from shortening to growth/pause) events, as well as the average amount of time spent by MTs in growth, shrinkage and pausing, MT lifetime and MT dynamicity (#of growth + shrinkage events/lifetime). Data are mean ± SEM from 3 independent experiments.
[a]$p < 0.05$.
[b]$p < 0.001$ by Student's t test.

Tubulin acetylation is required for MFN2-dependent regulation of mitochondrial motility but not for mitochondrial fusion or functional tethering to the ER

We observed that the co-localization of mitochondria with MTs was reduced in Mfn2 KO cells but restored when Mfn2 KO cells were treated with TSA (Figures S1E and S1F). No acetylated lys 105 miro1[40] was detected in either WT or Mfn2 KO MEFs and total miro1 appeared unchanged in Mfn2 KO cells, indicating that loss of acetylated or total miro1 did not underlie the defect in mitochondrial tethering to MTs (Figures S1G and S1H). We determined whether increasing acetylated tubulin levels by TSA reestablished regular mitochondria dynamics and/or mitochondrial associated ER-membrane (MAM) function, mitochondrial features affected by loss of MFN2 expression (Figure 2). We observed that TSA normalized both central and peripheral mitochondrial displacement velocity as well as mitochondria distribution in Mfn2 KO cells (Figures 2A–2C). However, while mitochondria elongated morphology was partially reestablished in Mfn2 KO cells treated with TSA, the HDAC inhibitor completely failed to recover mitochondria fusion, an activity significantly compromised in cells deprived of MFN2 (Figures 2D and 2E). Identical results were obtained using tubacin, a potent and selective HDAC6 inhibitor (Figures 2F–2I).[41]

We inquired whether the rescue of mitochondrial dynamics was dependent on acetylated tubulin or a general gain in MT stability resulting from tubulin acetylation. To test this, we adopted Iqgap1 KO MEFs, a cell line with normal MFN2 levels but naturally deprived of detyrosinated and acetylated MTs, two independent subsets of stable MTs[42] (Figure S2). By analogy with Mfn2 KO cells, we found that loss of IQGAP1 also resulted in defective MT and mitochondrial dynamics (Figure S3 and Table S2), consistent with a role for modified MTs in regulating mitochondria homeostasis. However, normalized detyrosinated tubulin levels by silencing tubulin tyrosine ligase (TTL) did not ameliorate mitochondrial dynamics to the extent of TSA treatment (Figures S3E–S3I), suggesting that rescue of mitochondria dynamics was dependent on the selective increase in acetylated tubulin rather than a general gain in MT stability (Figures S2 and S3 and Table S2).

Next, we tested the effects of restoring acetylated tubulin levels on loss of MAM function by analyzing the synthesis and transfer of phospholipid between ER and mitochondria, a known proxy of MAM activity, as well as changes in lipid classes by lipidomics analysis in Mfn2 KO cells.[5,43] MAM is a transient specialized subdomain of the ER with the characteristics of a lipid raft. The temporary formation of MAM domains in the ER regulates several metabolic pathways, including lipid and Ca^{2+} homeostasis and mitochondrial activity.[9,44] Alterations in the formation of MAM domains have been reported to induce significant changes in lipid metabolism in several pathologies including neurodegenerative disease.[10,44] In particular, defects in MAM activity have significant detrimental effects on the regulation of cholesterol and its esterification into cholesteryl esters.[45] Equally important, defects in MAM impair the regulation of sphingomyelin (SM) turnover and its hydrolysis into ceramide species.[46,47]

We found that Mfn2KO cells display significant increases in sphingomyelin and cholesterol with concomitant decreases in cholesteryl esters and ceramide levels (Figures 2J and 2K and Table S3) and that these changes could be rescued by TSA (Figures 2J and 2K). Conversely, TSA failed to normalize MAM-dependent phospholipid synthesis that we measured by incorporation of radiolabeled ^{3}H-Ser into newly synthesized ^{3}H-PtdSer (PS) and (H) ^{3}H-PtdEtn (PE) (Figure 2L).

Altogether, our results demonstrate a previously unrecognized role for MFN2 in the regulation of α-tubulin acetylation and suggest that this activity is important for MFN2-dependent control of mitochondria motility and lipid-raft MAM composition, but not for MFN2-dependent mitochondrial fusion or functional mitochondrial/ER tethering. Furthermore, our results in Iqgap1 KO cells support the notion that acetylated tubulin is a modulator of mitochondria dynamics *per se* and suggest that the machinery controlling mitochondria motility may regulate the α-tubulin acetylation cycle at sites of mitochondria contacts with MTs.
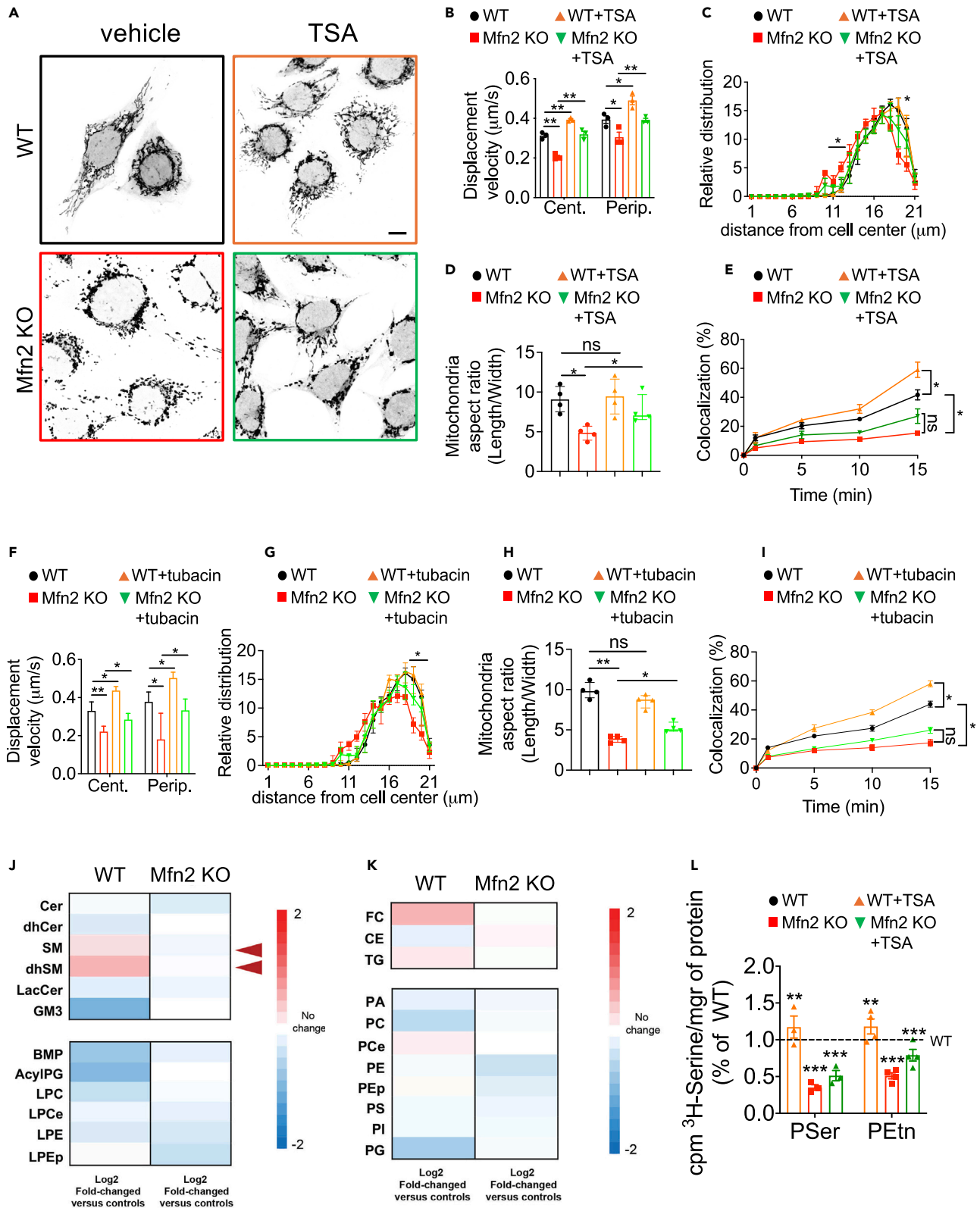
Figure 2. HDAC6 inhibition in Mfn2 KO MEFs rescues mitochondria motility and cholesterol esterification but not mitochondria fusion or phospholipid synthesis defects

(A) WT and Mfn2 KO cells were stained live with mitoTracker Red and treated with TSA (10 nM) or vehicle control for 6 h. Scale bar, 10 μm.

(B) Quantification of mitochondrial displacement velocity analyzed from movies acquired for 3 min (1f/2s) in cells treated as in A. Movies were analyzed using ImageJ manual tracking plug-in.

(C) Quantification of relative distribution of mitochondria (#) to the geometrical cell center in cells treated as in A.

(D) Quantification of mitochondria aspect ratio (length/width) in cells treated as in A (N = 100–120 mitochondria from 4 independent experiments).

(E) Quantification of mitochondria fusion using mitoDendra expression in cells treated as in A.

(F) Quantification of mitochondrial displacement velocity analyzed from movies acquired for 3 min (1f/2s) in cells treated with tubacin (20 μM). Movies were analyzed using ImageJ manual tracking plug-in (125–150 mitochondria/10–12 cells from 3 independent experiments).

(G) Quantification of relative distribution of mitochondria (#) to the geometrical cell center in cells treated with tubacin (20 μM).

(H) Quantification of mitochondria aspect ratio (length/width) in cells treated with tubacin (20 μM).

(I) Quantification of mitochondria fusion using mitoDendra expression in cells treated with tubacin or control vehicle for 6 h. (G,H and I) N = 125–150 mitochondria from 3 to 4 independent experiments.

(J and K) Heatmap representation of changes in lipid classes in MFN2 KO MEFs treated with vehicle control or TSA (10 nM).

(L) Phospholipid synthesis and transfer between ER and mitochondria in WT and Mfn2 KO MEFs treated with vehicle control or TSA (10 nM) for 6 h. Incorporation of ^{3}H-Ser into ^{3}H-PtdSer (PS) and (H) ^{3}H-PtdEtn (PE) after 2 h and 4 h expressed as % of the average value measured in the controls. Cer: ceramide, dhcer: dihydroceramide, SM: sphingomyelin, dhSM: dehydrosphingomyelin, GM3: monosialodihexosylganglioside. BMP: Bis(monoacylglycerol)phosphate, Acyl-PG, acylated phosphatidylglycerol, LPC: Lysophosphatidylcholine, LPCe: Lysophosphatidylcholine plasmalogen, LPE: Lysophosphatidylethanolamine, LPEp: Lysophosphatidylethanolamine plasmalogen; FC: free cholesterol, CE: cholesteryl esters; PA: phosphatidic acid; PC: Phosphatidylcholine; PCe Phosphatidylcholine plasmalogen; PE: Phosphatidylethanolamine; PEp: Phosphatidylethanolamine plasmalogen; PS: Phosphatidylserine; PI: Phosphatidylinositol; PG: Phosphatidylglycerol. *$p < 0.05$; **$p < 0.01$; ***$p < 0.001$; ns non-significant by Kruskal-Wallis test. Data are expressed as median with interquartile range.

MFN2 regulates tubulin acetylation by recruiting ATAT1 at sites of mitochondrial contacts with MTs

We began to investigate the mechanisms underlying MFN2 regulation of acetylated α-tubulin by measuring levels and localization of ATAT1 and HDAC6 in Mfn2 KO cells. HDAC6 expression was 3-fold higher in these cells, in contrast to ATAT1 levels, which remained unaffected (Figures S4A and S4B). Loss of MFN2 expression did not affect the percentage of cells in mitosis either (Figures S4C and S4D). However, when intracellular membranes were subjected to crude fractionation to isolate the cytosolic from the nuclear and ER fractions, unlike HDAC6 which remained mostly cytosolic, ATAT1 appeared in the cytosolic and in the nuclear/ER portion in WT cells but re-distributed more prominently to the nuclear/ER fraction in Mfn2 KO cells (Figures S4E and S4F). Accordingly, localization of endogenous ATAT1 with the mitochondria enriched fraction appeared to be decreased in Mfn2 KO cells compared to WT cells (Figures S4G and S4H).

We hypothesized that MFN2 may negatively regulate ATAT1 association with the ER by localizing ATAT1 to mitochondria outer membranes, and that this localization may facilitate the access of ATAT1 to openings of the MT lattice at sites of mitochondria contacts with MTs. High resolution confocal microscopy of endogenous proteins revealed punctuate localization of ATAT1 to mitochondria (∼0.5 ATAT1 foci per μm) and this co-localization was significantly reduced in cells deprived of MFN2 expression (Figures 3A–3C). Importantly, almost 80% of mitochondrially localized ATAT1 (∼60% of total ATAT1) also localized with endogenous MFN2, and ATAT1 decorated mitochondria were often observed to be in contact with MTs that appeared to be nicked (Figures 3D–3F, S5A, and S5B). Localization of ATAT1 to mitochondria was likely to be dependent on the association of MFN2 with an ATAT1 N-terminal fragment (1–242) inclusive of its catalytic domain, as demonstrated by the *in situ* validation of the endogenous interaction using the proximity ligation assay (Figures 3G and 3H), co-immunoprecipitation from cells overexpressing either full length Myc-MFN2/Flag-ATAT1 or either Myc-MFN2 or FLAG-ATAT1 alone (Figures 3I and S5C), and pull-down assays to map the site of binding using full-length or C-terminally truncated versions of Flag-ATAT1 and Myc-MFN2 (Figures 3I–3K). Lack of binding to TOMM20 or COX4, the subunit 4 of the inner mitochondrial enzyme cytochrome *c* oxidase, confirmed that the association with MFN2 was not due to non-specific stickiness of ATAT1 to mitochondria (Figure S5C).

Altogether, these data demonstrate that ATAT1 associates with mitochondria and that this localization is dependent on the binding of the catalytic domain of ATAT1 with MFN2.

Loss of acetylated tubulin may underlie CMT2A disease

Most MFN2 CMT mutations are missense, and all generate a dominant inheritance pattern, suggesting that mutations in MFN2 lead to either a gain of function or haploinsufficiency.[48,49] Furthermore, recent work supports the notion that restoring MNF1:MFN2 balance by increasing levels of its homologous protein MFN1 is a potential therapeutic approach for CMT2A.[17] The reason for this compensation is unclear, although both MFN2 and MFN1 have been implicated in mitochondria fusion. To determine the involvement of MFN2-dependent regulation of tubulin acetylation in CMT2A disease we investigated whether: 1) mutations in MFN2 affect the interaction with ATAT1 and/or fail to restore normal acetylated tubulin levels in Mfn2 KO cells; 2) MFN1 compensates for loss of MFN2 by restoring tubulin acetylation in Mfn2 KO cells; 3) loss of acetylated tubulin by MFN2 depletion is conserved in sensory neurons and sufficient to induce axonal fragmentation, a phenotype associated to axonal forms of CMT disease including CMT2A.

We found that MFN2 R94W and T105M, two of the most common N-terminal CMT mutations in MFN2[50–52] that do not lose their association with mitochondria (Figure S6A), bound to ATAT1 with higher affinity than WT MFN2 (Figures 4A–4C) and endogenous ATAT1 co-localized better with mutant MFN2 (although only with T105M to a significant degree) than WT MFN2 (Figures 4D and 4E). However,

A

B

C

D

E

F

G

PLA: ATAT1/MFN2

H

I

IP: Flag-ATAT1

IP: Myc-MFN2

J

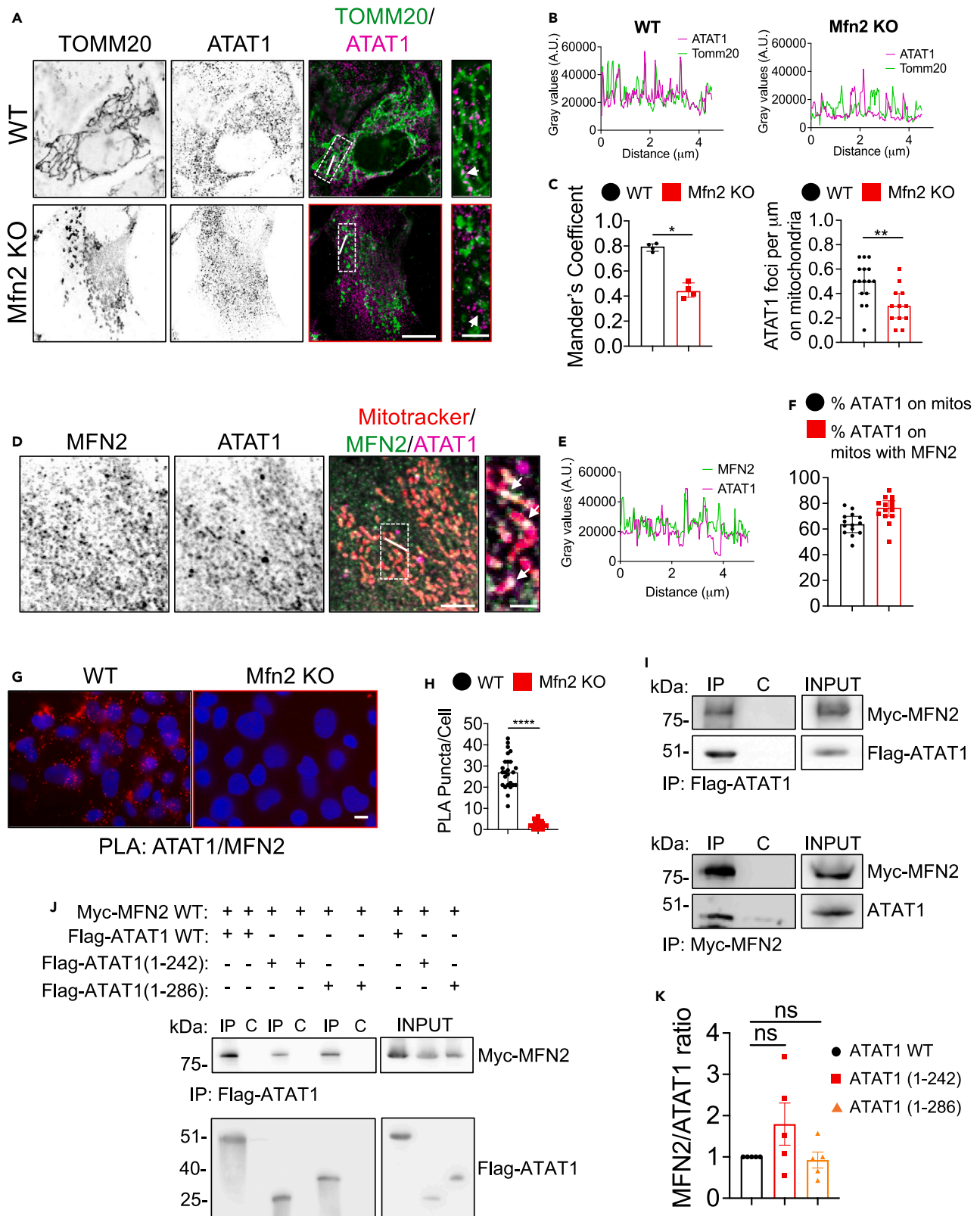| Myc-MFN2 WT: | + | + | + | + | + | + | + | + | + |
Flag-ATAT1 WT:	+	+	-	-	-	-	+	-	-
Flag-ATAT1(1-242):	-	-	+	+	-	-	-	+	-
Flag-ATAT1(1-286):	-	-	-	-	+	+	-	-	+

IP: Flag-ATAT1

K

Figure 3. MFN2 localizes ATAT1 to mitochondria outer membranes in MEFs

(A) Airyscan confocal images (single plane) of mitochondria (TOMM20) and ATAT1 in WT and Mfn2 KO MEFs. White arrows show localization of ATAT1 relative to TOMM20. Scale bar, 10 μm or 5 μm for zoomed image.

(B) Line scan analysis of mitochondria and ATAT1 localization from selected regions as in (A). Lines are shown as white bars on the merged image in (A).

(C) Quantification of localization of ATAT1 at mitochondria as in (A) by Mander's correlation coefficient. Number of ATAT1 foci on μm of mitochondria is also shown.

(D) Airyscan confocal images (single plane) of ATAT1 and MFN2 localization at mitochondria (Mito tracker red) in MEFs. White arrow heads show localization of MFN2 and ATAT1 on mitochondria. Scale bars, 5 μm and 2 μm for zoomed image.

(E) Line scan analysis of MFN2 and ATAT1 localization at mitochondria in WT cells.

(F) Quantification of ATAT1 signal localization at mitochondria and the fraction of this signal that co-localizes with MFN2 was calculated using ImageJ.

(G) Immunofluorescence analysis of MFN2 and ATAT1 PLA signal in WT and Mfn2 KO MEFs (confocal max projection image). Scale bar, 10 μm.

(H) Quantification of PLA puncta per cell in WT and Mfn2 KO MEFs.

(I) Interaction between ATAT1 and MFN2 was detected by immunoprecipitation (IP) followed by immunoblot analysis with the indicated antibodies (upper panel). Similarly, interaction between endogenous ATAT1 and transfected Myc-MFN2 WT was detected in HEK293T cells (lower panel).

(J) HEK293T cells were co-transfected with Myc-MFN2 WT and Flag-ATAT1 WT or Flag-ATAT1 (1–242) or Flag-ATAT1 (1–286). Interaction between MFN2 and ATAT1 WT or mutants was detected by co-immunoprecipitation followed by immunoblot analysis with the indicated antibodies.

(K) Normalized MFN2 to ATAT1 signal ratio from (J) was plotted. Data are expressed as median with interquartile range. N = 35–50 cells from 3 to 4 independent experiments. *$p < 0.05$; ****$p < 0.001$; ns non-significant by Mann–Whitney U test (C and H) and Kruskal-Wallis test (K).

both mutations failed to rescue normal acetylated tubulin levels when expressed in Mfn2 KO cells (Figures 4F and 4G). This result was in stark contrast with ectopic expression of MFN1, which was fully able to compensate for loss of MFN2 on acetylated tubulin levels in Mfn2 KO cells (Figures 4H and 4I). We examined the effects of overexpressing WT and mutant MFN2 or WT MFN1 on HDAC6 protein levels in MFN2 KO cells and found that while only WT MFN2 normalized them, WT MNF1 expression had no significant impact (Figures S6B and S6C). In addition, complete loss of MFN1 expression in MFN1 KO MEFs caused ∼50% reduction in tubulin acetylation but no significant alteration of either ATAT1 or HDAC6 protein levels (Figures S6D–S6G), implying that modulation of HDAC6 could not be the only mechanism underlying MFN-mediated regulation of tubulin acetylation.

A complex between miro/Milton (TRAK) and MFN2 has been previously shown,[14] and miro is implicated in the regulation of MFN2-dependent mitochondrial fusion in response to mitochondrial Ca^{2+} concentration.[14] We tested whether also ATAT1 interacted with miro and/or kinesin heavy chain (Kif5c) and determined the potential effects of mutant MFN2 on the formation of these complexes. By proximity ligation assays, we detected association between endogenous ATAT1 and Miro1 in WT MEFs and this association was significantly disrupted in Mfn2 KO MEFs (Figures S6H and S6I). We also found that ectopic ATAT1 co-immunoprecipitated with both endogenous miro2 and kif5c and that ectopic expression of mutant MFN2 R94W or T105M significantly lowered the affinity of these bindings (Figures 4J–4M).

Taken together, these data demonstrate that regulation of acetylated tubulin is an activity shared by MFN1 and that loss of acetylated tubulin may play a primary role in CMT2A via the sequestering effect of MFN2 mutations on ATAT1 from miro and kif5c binding.

These observations became particularly meaningful when we tested the consequences of loss of MFN2 in sensory neurons and the effects of HDAC6 inhibition on these phenotypes. By analogy with Mfn2 KO cells, silencing of MFN2 expression reduced acetylated tubulin levels both in adult mouse DRG neurons grown in culture and in cell bodies of somatosensory neurons of third instar stage *Drosophila* larvae (Figures 5A–5E). Similar to Mfn2 KO MEFs, we observed localization of endogenous ATAT1 and MFN2 in DRG neurons (Figures S7A–S7C) and significant reduction in the extent of ATAT1 localization to mitochondrial membranes in neurons silenced for Mfn2 expression in both proximal and distal portion of the axon (Figures S7D–S7F). Importantly, cultured sensory neurons deprived of MFN2 acquired a dying-back degeneration phenotype starting from distal regions of the axon, as indicated by the appearance of retraction bulbs at the onset of axonal fragmentation (Figures 5F and 5G). We observed that loss of acetylated tubulin preceded axonal degeneration in DRG neurons deprived of MFN2 for shorter times (Figures S7G–S7J) and that HDAC6 inhibition, which significantly rescued normal acetylated tubulin levels in Mfn2 KD neurons, prevented both retraction bulb formation and axonal degeneration in neurons deprived of MFN2, while having only negligible effects on WT controls (Figures 5H–5J). Notably, a role for any HDAC6 substrate other than tubulin was ruled out by inducing rescue in Mfn2 depleted DRG neurons with expression of ATAT1 localized to mitochondrial outer membranes by fusion with the OMP25 targeting sequence (Figures S8A and S8B).[53] In addition, while neither MFN2 CMT2A mutants could compensate for MFN2 loss on axonal degeneration, both mutants were sufficient to induce about 2.5-fold increase in axonal degeneration if expressed in control DRG neurons in the absence of HDAC6 inhibition (Figures S8C–S8F).

Altogether, these findings indicate that MFN2 dependent recruitment of ATAT1 to sites of mitochondrial contacts with MTs is conserved in sensory neurons and required for axonal integrity by maintaining normal levels of MT acetylation. Taking consideration of our functional data in MEF cells, and consistent with previous observations in cellular models of CMT2 caused by MFN2 mutations, these results also suggest that distal axonal degeneration caused by mutant MFN2 predominantly depends on loss of acetylated tubulin due to mutant MFN2-mediated high jacking of ATAT1, which affects mitochondrial motility and distribution, but not on the loss of fusion or functional mitochondria/ER tethering.

DISCUSSION

MFN2 mutations in CMT2A disrupt the fusion[54] of mitochondria and compromise ER-mitochondrial interactions.[5,35] However, while certain CMT2A mutant forms of MFN2 impair mitochondrial fusion and/or functional mitochondria/ER tethering, others do not affect either function,[54] casting doubt on the implication of these MFN2 activities in the etiology of CMT2.
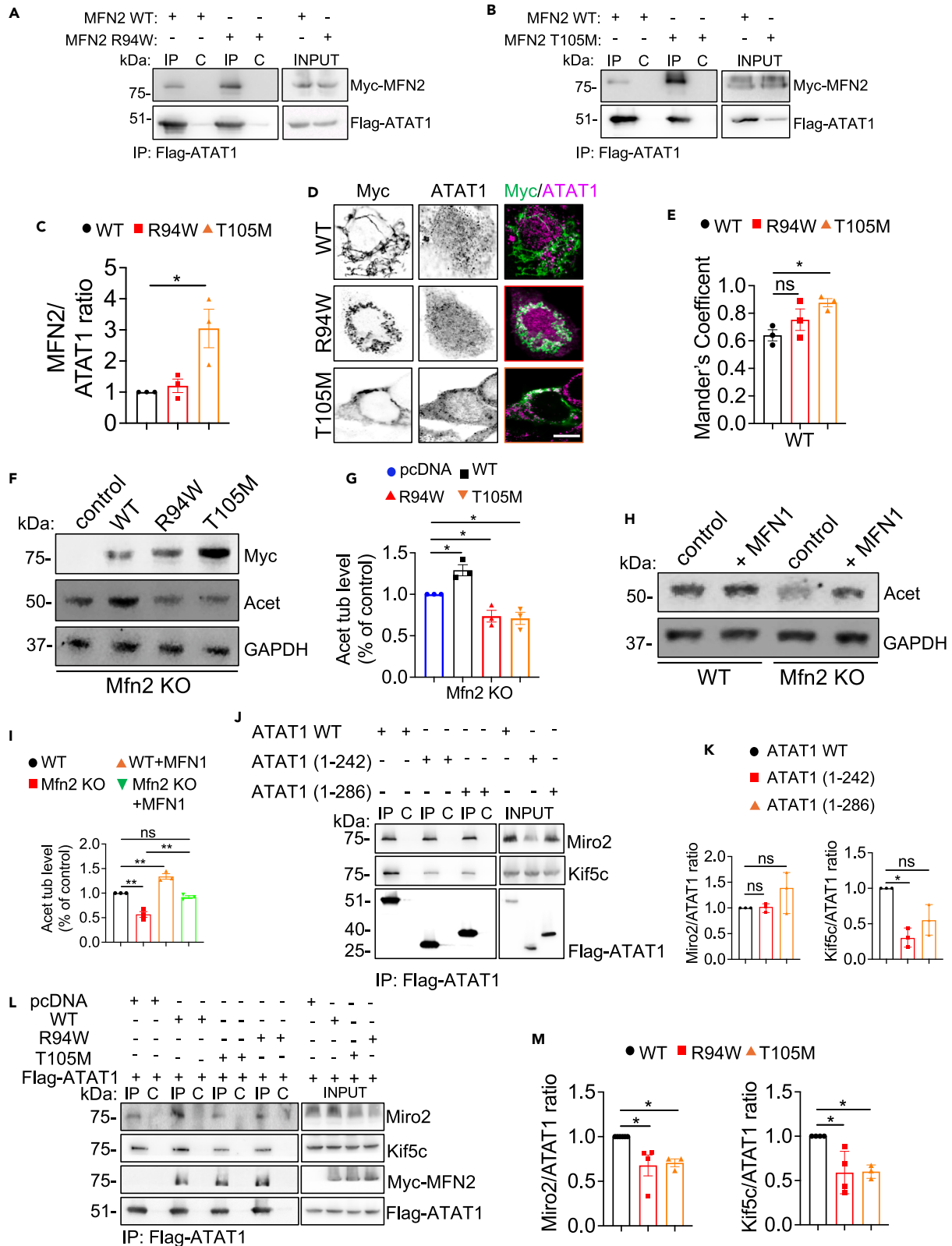
Figure 4. Regulation of α-tubulin acetylation by MFN2 is affected by MFN2 mutations and shared by MFN1

(A) HEK293T cells were co-transfected with Flag-ATAT1 and Myc-MFN2 WT or Myc-MFN2 R94W.

(B) HEK293T cells were co-transfected with Flag-ATAT1 and Myc-MFN2 WT or Myc-MFN2 T105M. Interaction between ATAT1 WT and MFN2 WT or mutants was detected by immunoprecipitation (IP) followed by immunoblot (IB) with the indicated antibodies.

(C) The ratio of the MFN2 signal to the ATAT1 signal from (A and B) was plotted.

(D) Representative confocal immunofluorescence images (max projections from z-stacks) overexpressing Myc-MFN2 WT, Myc-MFN2 R94W, Myc-MFN2 T105M in WT MEF cells (n = 25–30 cells). Scale bar 10 μm.

(E) Mander's coefficient analysis for WT MEF cells co transfected with Myc-MFN2 WT, Myc-MFN2 R94W and Myc-MFN2 T105M.

(F) Representative immunoblot of acetylated tubulin levels in Mfn2 KO cells co-transfected with Myc-MFN2 WT, Myc-MFN2 R94W and Myc-MFN2 T105M.

(G) Quantification of acetylated tubulin levels expressed as % of control levels from 3 independent experiments as in F. (H) Representative immunoblot of acetylated tubulin levels in MFN1 overexpressing WT and Mfn2 KO cells. (I) Quantification of acetylated tubulin levels expressed as % of control levels from 4 independent experiments as in H. (J) Interaction between ATAT1 or its truncated mutants (1–242; 1–286) and endogenous Miro2 or Kif5c was detected in HEK293T cells transfected with Flag-ATAT1 WT or its truncated mutants. (K) The ratio of the Miro2 and Kif5c signal to the ATAT1 signal from (J) was plotted. (L) Interaction between Flag-ATAT1 and endogenous Miro2 or Kif5c was detected in HEK293T cells in presence or absence of Myc-MFN2 WT, Myc-MFN2 R94W and Myc-MFN2 T105M. (M) The ratio of the Miro2 and Kif5c signal to the ATAT1 signal from (L) is plotted. Data are expressed as median with interquartile range. n = 3–4 independent experiments. *$p \leq 0.05$, **$p < 0.01$; ns non-significant by Kruskal-Wallis test.

In this study we report that MFN2 is a regulator of α-tubulin acetylation and MT dynamics, and that in Mfn2 KO MEFs, rescuing α-tubulin acetylation levels by pharmacological inhibition of HDAC6 corrects defects in MT dynamics and mitochondrial motility and some MAM functions, but not MAM integrity or mitochondrial fusion.

It is thought that in neurons a large pool of the α-tubulin acetyltransferase ATAT1 is recruited to the MT lattice by vesicle "hitchhiking" prior to entering the lumen at MT ends or at cracks in the MT lattice.[55–58] In migrating cells, clathrin-coated pits control MT acetylation through a direct interaction of ATAT1 with the clathrin adaptor AP2.[59] The rules dictating the selection of the docking sites on vesicles, clathrin-coated pits or MTs are however unknown. Similarly unexplored is whether other organelles can act as docking sites for ATAT1 binding. These are important questions to address, as either hypoacetylation or hyperacetylation of tubulin are predicted to negatively affect MT-dependent functions, either by reducing the local flexibility of the MT (thus promoting further breakage upon bending) or by inhibiting MT dynamics while promoting premature tubulin longevity.

Herein, we show that in addition to modulation of HDAC6 protein levels, regulation of tubulin acetylation by MFN2 occurs through MFN2-mediated recruitment of ATAT1 to OMMs, an activity: (1) conserved in sensory neurons, (2) critical for the induction of axonal degeneration by MFN2 loss of function, and (3) impaired in two MFN2 mutants associated with CMT2A. Interestingly, the binding of MFN2 to ATAT1 is dependent on the N-terminal catalytic domain of ATAT1 and the same domain is also necessary for the association of ATAT1 with kinesin-1 but not with miro, a Rho-GTPase implicated in the regulation of mitochondrial transport by linking mitochondria outer membranes to kinesin and dynein motors.[60,61] Conversely, both MFN2 R94W and T105M mutants disrupt the binding of ATAT1 with either miro or kinesin-1, and an endogenous ATAT1/miro complex fails to form in cells deprived of MFN2 expression, suggesting that while ATAT1 binding to miro may not depend on kinesin, the formation of a stable ATAT1/miro/kinesin-1 complex relies on WT MFN2. Based on these observations, we propose that, in analogy to axonal vesicles,[57] mitochondria contacts with MTs are hotspots of tubulin acetylation and that this function is impaired in CMT2 disease caused by MFN2 mutations.

MTs are a subset of stable MTs with key roles in the regulation of axonal transport and mitochondrial dynamics. Along with providing preferential tracks for kinesin-1- and dynein-dependent mitochondria transport, their stability and flexibility make them uniquely adapted to sustain mechanical stress caused by surface tension and organelle/organelle interactions.[30,32,62] We found that mutant R94W or T105M MFN2 cannot compensate for loss of MFN2 expression on either acetylated tubulin levels and axonal degeneration, and that expressing either MFN2 mutants is sufficient to induce axonal damage in WT DRG neurons. We propose that in CMT2A disease, mutant MFN2 drives axonal degeneration by disrupting the ability of mitochondria to release ATAT1 at specific sites on axonal MTs, leading to an imbalance in tubulin acetylation with consequent impairment of mitochondrial transport. Our findings also provide evidence that the release of ATAT1 by MFN2 depends on the formation of a stable ATAT1/miro/kinesin-1 complex, which may be necessary to allow discharge of ATAT1 at putative entry sites into the MT lattice. This is in line with the observation that motors can leave marks in the MT shaft by inducing breaks in the lattice and promote MT self-repair.[36,38,39] Further work is required to understand the rules of site selection and whether a break in the MT lattice is sufficient to induce ATAT1 release from MFN2 through a putative conformational change in the motor complex.

We found that HDAC6 inhibition rescues the defect in MAM-dependent cholesterol and SM metabolism assayed by cellular lipidomic analysis but fails to normalize MAM-dependent phospholipid synthesis measured by incorporation of 3H-Ser into 3H-PtdSer (PS) and (H) 3H-PtdEtn (PE). We note that the activation of MAM, as a lipid raft, is strictly dependent on its enrichment on cholesterol and sphingomyelin levels, as well as the reorganization of ceramide and phospholipids with different saturation degrees. Our data indicate that the regulation of all these lipid classes is altered in Mfn2 KO cells, and that the levels of cholesterol and SM are rescued by HDAC inhibition, but not those of specific phospholipids that are indispensable for the correct control of MAM functions. Indeed, HDAC6 inhibitors, and in particular TSA, were reported to modulate the expression of genes involved in cholesterol synthesis, uptake and efflux and to restore cholesterol redistribution in models of neurodegenerative disorders such as Niemann-Pick's disease.[63] Thus, in the context of Mfn2 ablation, TSA could rescue cholesterol efflux and SM turnover by this mechanism. However, we posit that the limited impact of TSA on the restoration of the lipid structure of the MAM, precludes the total rescue of MAM activities such as phosphatidylserine synthesis and transfer to mitochondria.
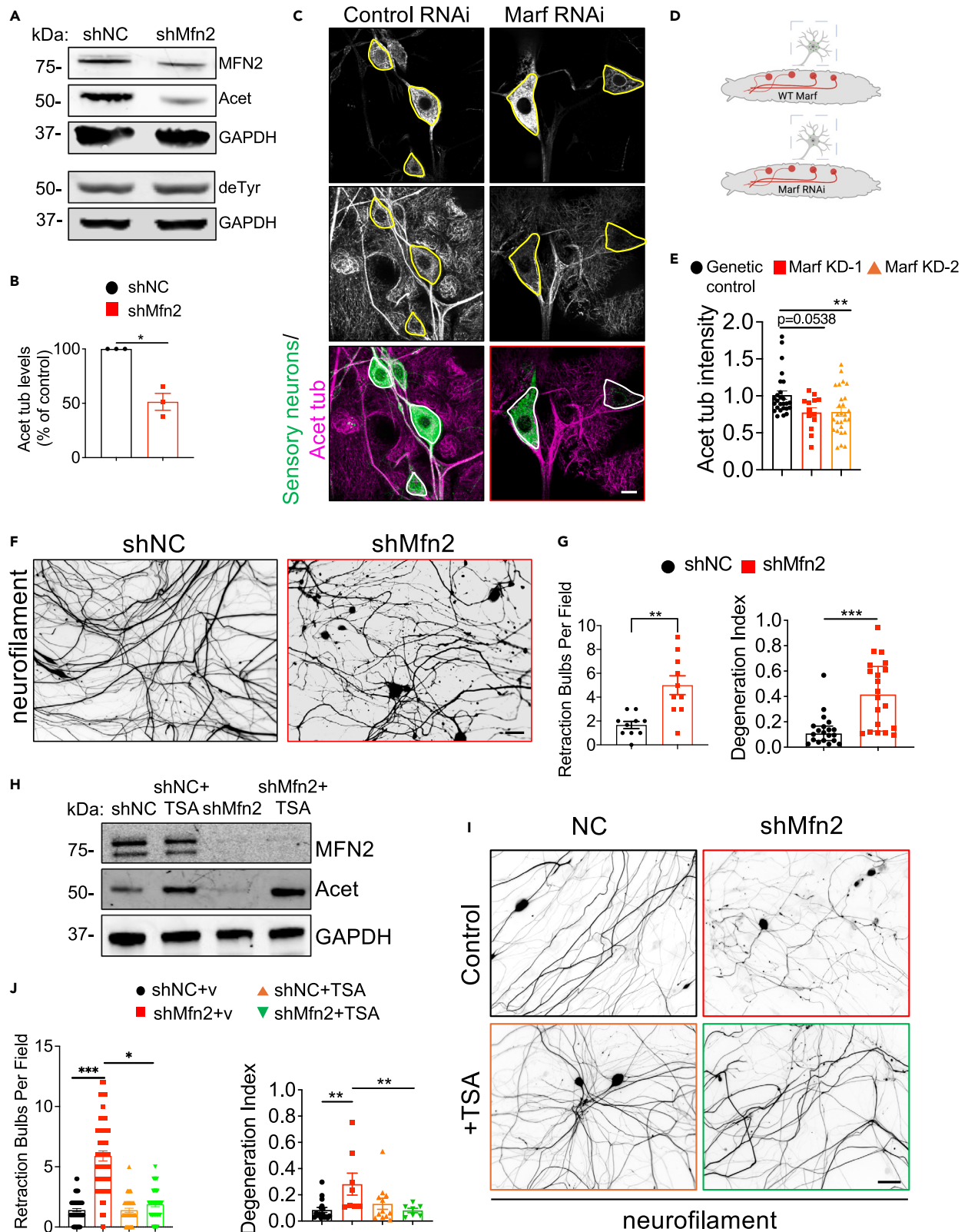
Figure 5. MFN2 regulates α-tubulin acetylation in sensory neurons *in vitro* and *in vivo* and this activity is required for axonal integrity

(A) Representative immunoblot of MFN2, acetylated (Acet) and detyrosinated tubulin (deTyr) levels in adult DRG neurons (14 DIV) silenced of Mfn2 expression at 7 DIV. GAPDH, loading control.

(B) Quantification of acetylated tubulin staining in MFN2 depleted DRG neurons relative to control neurons infected with shNC (non-coding shRNA).

(C) Representative confocal immunofluorescence images (max projections from z-stacks) of late third-instar larvae in control RNAi and MarfKD. Multi-dendritic neuron driver 109(2)80 Gal4 driver was used to label *Drosophila* larval somatosensory neurons (CD8-GFP).

(D) Cartoon image of WT Marf and MarfRNAi late third-instar larvae.

(E) Quantification of acetylated tubulin in somatosensory neurons as in C. Two different strategies were used, Marf KD-1 (BL 67158) and KD-2 (BL 31157).

(F) Images of representative fields showing dissociated adult DRG neurons (14 DIV) treated as in A, fixed and immunostained with mouse anti-neurofilament (2H3-s) antibody.

(G) Quantification of number of retraction bulbs per field and degree of axonal degeneration. The area occupied by the axons (total axonal area) and degenerating axons (fragmented axonal area) was measured in the same field from images in WT and MFN2 KD DRG neurons. Degeneration index was calculated as the ratio between fragmented axonal area and total axonal area.

(H) Representative immunoblot of MFN2, acetylated tubulin (Acet) levels in control (shNC) and MFN2 (shMFN2) silenced DRG neurons incubated with 10 nM of the HDAC6 inhibitor TSA or vehicle control for 6 h prior to lysis. GAPDH, loading control.

(I) Representative widefield immunofluorescence images of DRG neurons treated as in H.

(J) Quantification of number of retraction bulbs per field and degree of axonal degeneration in DRG neurons treated as in H prior to fixation and staining. Data are represented as median and interquartile range from 3 independent experiments. *$p < 0.05$; **$p < 0.01$, ***$p < 0.001$ by Mann-Whitney U test (B, E and G) and Kruskal-Wallis test (J). Scale bars, 5 μm (C); 50 μm (F, I).

By combining our observations in Mfn2 KO MEFs and KD sensory neurons, we propose that axonal degeneration caused by MFN2 loss of function mutations may not depend on impaired mitochondrial fusion or functional mitochondria/ER tethering, but rather on loss of MFN2-dependent regulation of mitochondrial transport by interfering with ATAT1-dependent tubulin acetylation at sites of mitochondria and MT contact. Our interpretation is consistent with a pathogenic role for disrupted mitochondrial transport in neuropathies and a key role for tubulin acetylation in mitochondrial dynamics. Indeed, multiple studies report that axonal degeneration precedes cell body death in several peripheral neuropathies, including CMT disease. Mitochondria are the principal mediators of ATP production and Ca^{2+} buffering, and they actively distribute to areas of high energy demand and Ca^{2+} flux within the axon.[14,15] A defect in mitochondria translocation to these sites would be expected to lead to preferential degeneration of long axons that more frequently experience fluctuations in ATP and Ca^{2+} levels.

Several lines of evidence support a role for perturbation of acetylated tubulin levels in CMT2A: 1) mutant MFN2 (MFN2R94Q) knock-in mice lack acetylated tubulin in distal axons of their long peripheral nerves[22]; 2) HDAC6 inhibition has been reported to be a promising therapeutic approach in several toxic and familial peripheral neuropathies, including CMT2A[22]; 3) the formin INF2, mutations of which cause dominant intermediate CMT in association with FSGS,[64] is a positive regulator of tubulin acetylation by modulating ATAT1 transcription. We note, however, that HDAC6 deacetylates additional lysine residues of α- and β-tubulin and has multiple substrates in addition to tubulin, casting doubt on the specificity of this approach. Conversely, tubulin is one of the only two substrates for ATAT1, in addition to cortactin.[65] Furthermore, the structure of ATAT1 provides a unique scaffold for designing small molecule modulators of tubulin acetylation for therapeutic use.[66] In particular, the identification of ATAT1 mutations that decrease or increase ATAT1 activity suggests that small molecule compounds could be identified to increase or decrease ATAT1 activity to stabilize or destabilize MTs for therapeutic purposes.[66] Taken together, these studies indicate that targeting ATAT1 activity or expression may represent an alternative and more specific therapeutic approach aimed at restoring sensory neuron function in CMT2A and perhaps other related CMT subtypes.

Limitations of the study

We acknowledge that our study, except for the Mfn2 KD fly model, is limited to observations in immortalized cells and adult primary DRG neurons. Further work is warranted to evaluate whether ATAT1-mediated rescue of tubulin acetylation and axonal degeneration also occurs *in vivo*, using preclinical models of neuropathy in which loss of acetylated tubulin in peripheral neurons has been reported. Another limitation relates to the use of ectopic expression of ATAT1 to normalize loss of MFN2 expression. Development of small molecule ATAT1 activators will provide a better strategy to adopt in mechanistic as well as preclinical studies.

STAR★METHODS

Detailed methods are provided in the online version of this paper and include the following:

- KEY RESOURCES TABLE
- RESOURCE AVAILABILITY
  - Lead contact
  - Materials availability
  - Data and code availability
- EXPERIMENTAL MODEL AND STUDY PARTICIPANT DETAILS
  - Mice for primary cell cultures
  - Drosophila melanogaster
  - Cell lines

- METHOD DETAILS
  - Confocal microscopy and analysis
  - Airyscan confocal microscopy and analysis
  - Western blot analysis
  - Proximity ligation assay (PLA)
  - Analysis of mitochondrial morphology, motility and distribution
  - Microtubule dynamics
  - Mitodendra
  - Lentivirus production
  - Retrovirus production
  - MT stability
  - Analysis of phospholipid synthesis in cultured cells
  - Lipidomics
  - Cellular fractionation
  - Isolation of adult DRG neurons
  - Degeneration index in DRG neurons
  - Immunolabeling of *Drosophila* larvae
  - Imaging and quantification of *Drosophila* sensory neurons
  - Co-immunoprecipitation assay
- QUANTIFICATION AND STATISTICAL ANALYSIS

SUPPLEMENTAL INFORMATION

Supplemental information can be found online at https://doi.org/10.1016/j.isci.2024.109994.

AUTHOR CONTRIBUTIONS

F.B. and A.K. conceptualized the study and crafted the manuscript. D.L., M.E.P., P.I., M.C., G.J.S., and V.V.E. conducted experiments and produced primary data. F.B., P.I., L.D.M., W.B.G., and E.A.G. oversaw data analysis and experimental procedures. Additionally, P.I., L.D.M., and E.A.G. offered valuable insights and contributed essential techniques.

DECLARATION OF INTERESTS

The authors declare no competing interests.

REFERENCES

1. Morena, J., Gupta, A., and Hoyle, J.C. (2019). Charcot-Marie-Tooth: From Molecules to Therapy. Int. J. Mol. Sci. *20*, 3419. https://doi.org/10.3390/ijms20143419.

2. Feely, S.M.E., Laura, M., Siskind, C.E., Sottile, S., Davis, M., Gibbons, V.S., Reilly, M.M., and Shy, M.E. (2011). MFN2 mutations cause severe phenotypes in most patients with CMT2A. Neurology *76*, 1690–1696. https://doi.org/10.1212/WNL.0b013e31821a441e.

3. Dorn, G.W., 2nd (2020). Mitofusin 2 Dysfunction and Disease in Mice and Men. Front. Physiol. *11*, 782. https://doi.org/10.3389/fphys.2020.00782.

4. Filadi, R., Pendin, D., and Pizzo, P. (2018). Mitofusin 2: from functions to disease. Cell Death Dis. *9*, 330. https://doi.org/10.1038/s41419-017-0023-6.

5. Larrea, D., Pera, M., Gonnelli, A., Quintana-Cabrera, R., Akman, H.O., Guardia-Laguarta, C., Velasco, K.R., Area-Gomez, E., Dal Bello, F., De Stefani, D., et al. (2019). MFN2 mutations in Charcot-Marie-Tooth disease alter mitochondria-associated ER membrane function but do not impair bioenergetics. Hum. Mol. Genet. *28*, 1782–1800. https://doi.org/10.1093/hmg/ddz008.

6. Baloh, R.H., Schmidt, R.E., Pestronk, A., and Milbrandt, J. (2007). Altered axonal mitochondrial transport in the pathogenesis of Charcot-Marie-Tooth disease from mitofusin 2 mutations. J. Neurosci. *27*, 422–430. https://doi.org/10.1523/JNEUROSCI.4798-06.2007.

7. Schiavon, C.R., Shadel, G.S., and Manor, U. (2021). Impaired Mitochondrial Mobility in Charcot-Marie-Tooth Disease. Front. Cell Dev. Biol. *9*, 624823. https://doi.org/10.3389/fcell.2021.624823.

8. Palau, F., Estela, A., Pla-Martín, D., and Sánchez-Piris, M. (2009). The role of

mitochondrial network dynamics in the pathogenesis of Charcot-Marie-Tooth disease. Adv. Exp. Med. Biol. *652*, 129–137. https://doi.org/10.1007/978-90-481-2813-6_9.

9. Cosson, P., Marchetti, A., Ravazzola, M., and Orci, L. (2012). Mitofusin-2 independent juxtaposition of endoplasmic reticulum and mitochondria: an ultrastructural study. PLoS One *7*, e46293. https://doi.org/10.1371/journal.pone.0046293.

10. Filadi, R., Greotti, E., Turacchio, G., Luini, A., Pozzan, T., and Pizzo, P. (2015). Mitofusin 2 ablation increases endoplasmic reticulum-mitochondria coupling. Proc. Natl. Acad. Sci. USA *112*, E2174–E2181. https://doi.org/10.1073/pnas.1504880112.

11. Filadi, R., Theurey, P., and Pizzo, P. (2017). The endoplasmic reticulum-mitochondria coupling in health and disease: Molecules, functions and significance. Cell Calcium *62*, 1–15. https://doi.org/10.1016/j.ceca.2017.01.003.

12. Han, S., Zhao, F., Hsia, J., Ma, X., Liu, Y., Torres, S., Fujioka, H., and Zhu, X. (2021). The role of Mfn2 in the structure and function of endoplasmic reticulum-mitochondrial tethering in vivo. J. Cell Sci. *134*, jcs253443. https://doi.org/10.1242/jcs.253443.

13. Bassot, A., Prip-Buus, C., Alves, A., Berdeaux, O., Perrier, J., Lenoir, V., Ji-Cao, J., Berger, M.A., Loizon, E., Cabaret, S., et al. (2021). Loss and gain of function of Grp75 or mitofusin 2 distinctly alter cholesterol metabolism, but all promote triglyceride accumulation in hepatocytes. Biochim. Biophys. Acta. Mol. Cell Biol. Lipids *1866*, 159030. https://doi.org/10.1016/j.bbalip.2021.159030.

14. Misko, A., Jiang, S., Wegorzewska, I., Milbrandt, J., and Baloh, R.H. (2010). Mitofusin 2 Is Necessary for Transport of Axonal Mitochondria and Interacts with the Miro/Milton Complex. J. Neurosci. *30*, 4232–4240. https://doi.org/10.1523/Jneurosci.6248-09.2010.

15. Misko, A.L., Sasaki, Y., Tuck, E., Milbrandt, J., and Baloh, R.H. (2012). Mitofusin2 mutations disrupt axonal mitochondrial positioning and promote axon degeneration. J. Neurosci. *32*, 4145–4155. https://doi.org/10.1523/JNEUROSCI.6338-11.2012.

16. Mou, Y., Dein, J., Chen, Z., Jagdale, M., and Li, X.J. (2021). MFN2 Deficiency Impairs Mitochondrial Transport and Downregulates Motor Protein Expression in Human Spinal Motor Neurons. Front. Mol. Neurosci. *14*, 727552. https://doi.org/10.3389/fnmol.2021.727552.

17. Zhou, Y., Carmona, S., Muhammad, A.K.M.G., Bell, S., Landeros, J., Vazquez, M., Ho, R., Franco, A., Lu, B., Dorn, G.W., 2nd, et al. (2019). Restoring mitofusin balance prevents axonal degeneration in a Charcot-Marie-Tooth type 2A model. J. Clin. Invest. *129*, 1756–1771. https://doi.org/10.1172/JCI124194.

18. Kalebic, N., Sorrentino, S., Perlas, E., Bolasco, G., Martinez, C., and Heppenstall, P.A. (2013). alphaTAT1 is the major alpha-tubulin acetyltransferase in mice. Nat. Commun. *4*, 1962. https://doi.org/10.1038/ncomms2962.

19. Morley, S.J., Qi, Y., Iovino, L., Andolfi, L., Guo, D., Kalebic, N., Castaldi, L., Tischer, C., Portulano, C., Bolasco, G., et al. (2016). Acetylated tubulin is essential for touch sensation in mice. Elife *5*, e20813. https://doi.org/10.7554/eLife.20813.

20. Yan, C., Wang, F., Peng, Y., Williams, C.R., Jenkins, B., Wildonger, J., Kim, H.J., Perr, J.B., Vaughan, J.C., Kern, M.E., et al. (2018). Microtubule Acetylation Is Required for Mechanosensation in Drosophila. Cell Rep. *25*, 1051–1065.e6. https://doi.org/10.1016/j.celrep.2018.09.075.

21. Van Helleputte, L., Kater, M., Cook, D.P., Eykens, C., Rossaert, E., Haeck, W., Jaspers, T., Geens, N., Vanden Berghe, P., Gysemans, C., et al. (2018). Inhibition of histone deacetylase 6 (HDAC6) protects against vincristine-induced peripheral neuropathies and inhibits tumor growth. Neurobiol. Dis. *111*, 59–69. https://doi.org/10.1016/j.nbd.2017.11.011.

22. Picci, C., Wong, V.S.C., Costa, C.J., McKinnon, M.C., Goldberg, D.C., Swift, M., Alam, N.M., Prusky, G.T., Shen, S., Kozikowski, A.P., et al. (2020). HDAC6 inhibition promotes alpha-tubulin acetylation and ameliorates CMT2A peripheral neuropathy in mice. Exp. Neurol. *328*, 113281. https://doi.org/10.1016/j.expneurol.2020.113281.

23. Tran, A.D.A., Marmo, T.P., Salam, A.A., Che, S., Finkelstein, E., Kabarriti, R., Xenias, H.S., Mazitschek, R., Hubbert, C., Kawaguchi, Y., et al. (2007). HDAC6 deacetylation of tubulin modulates dynamics of cellular adhesions. J. Cell Sci. *120*, 1469–1479. https://doi.org/10.1242/jcs.03431.

24. Valenzuela-Fernandez, A., Cabrero, J.R., Serrador, J.M., and Sanchez-Madrid, F. (2008). HDAC6: a key regulator of cytoskeleton, cell migration and cell-cell interactions. Trends Cell Biol. *18*, 291–297. https://doi.org/10.1016/j.tcb.2008.04.003.

25. Akella, J.S., Wloga, D., Kim, J., Starostina, N.G., Lyons-Abbott, S., Morrissette, N.S., Dougan, S.T., Kipreos, E.T., and Gaertig, J. (2010). MEC-17 is an alpha-tubulin acetyltransferase. Nature *467*, 218–222. https://doi.org/10.1038/nature09324.

26. Shida, T., Cueva, J.G., Xu, Z., Goodman, M.B., and Nachury, M.V. (2010). The major alpha-tubulin K40 acetyltransferase alphaTAT1 promotes rapid ciliogenesis and efficient mechanosensation. Proc. Natl. Acad. Sci. USA *107*, 21517–21522. https://doi.org/10.1073/pnas.1013728107.

27. d'Ydewalle, C., Krishnan, J., Chiheb, D.M., Van Damme, P., Irobi, J., Kozikowski, A.P., Vanden Berghe, P., Timmerman, V., Robberecht, W., and Van Den Bosch, L. (2011). HDAC6 inhibitors reverse axonal loss in a mouse model of mutant HSPB1-induced Charcot-Marie-Tooth disease. Nat. Med. *17*, 968–974. https://doi.org/10.1038/nm.2396.

28. L'Hernault, S.W., and Rosenbaum, J.L. (1985). Chlamydomonas alpha-tubulin is posttranslationally modified by acetylation on the epsilon-amino group of a lysine. Biochemistry *24*, 473–478. https://doi.org/10.1021/bi00323a034.

29. LeDizet, M., and Piperno, G. (1987). Identification of an acetylation site of Chlamydomonas alpha-tubulin. Proc. Natl. Acad. Sci. USA *84*, 5720–5724. https://doi.org/10.1073/pnas.84.16.5720.

30. Portran, D., Schaedel, L., Xu, Z., Théry, M., and Nachury, M.V. (2017). Tubulin acetylation protects long-lived microtubules against mechanical ageing. Nat. Cell Biol. *19*, 391–398. https://doi.org/10.1038/ncb3481.

31. Schaedel, L., John, K., Gaillard, J., Nachury, M.V., Blanchoin, L., and Théry, M. (2015). Microtubules self-repair in response to mechanical stress. Nat. Mater. *14*, 1156–1163. https://doi.org/10.1038/nmat4396.

32. Janke, C., and Montagnac, G. (2017). Causes and Consequences of Microtubule Acetylation. Curr. Biol. *27*, R1287–R1292. https://doi.org/10.1016/j.cub.2017.10.044.

33. Barlan, K., and Gelfand, V.I. (2010). Intracellular transport: ER and mitochondria meet and greet along designated tracks. Curr. Biol. *20*, R845–R847. https://doi.org/10.1016/j.cub.2010.08.058.

34. Rowland, A.A., and Voeltz, G.K. (2012). Endoplasmic reticulum-mitochondria contacts: function of the junction. Nat. Rev. Mol. Cell Biol. *13*, 607–625. https://doi.org/10.1038/nrm3440.

35. de Brito, O.M., and Scorrano, L. (2008). Mitofusin 2 tethers endoplasmic reticulum to mitochondria. Nature *456*, 605–610. https://doi.org/10.1038/nature07534.

36. Aumeier, C., Schaedel, L., Gaillard, J., John, K., Blanchoin, L., and Théry, M. (2016). Self-repair promotes microtubule rescue. Nat. Cell Biol. *18*, 1054–1064. https://doi.org/10.1038/ncb3406.

37. Atherton, J., Stouffer, M., Francis, F., and Moores, C.A. (2018). Microtubule architecture in vitro and in cells revealed by cryo-electron tomography. Acta Crystallogr. D Struct. Biol. *74*, 572–584. https://doi.org/10.1107/S2059798318001948.

38. Triclin, S., Inoue, D., Gaillard, J., Htet, Z.M., DeSantis, M.E., Portran, D., Derivery, E., Aumeier, C., Schaedel, L., John, K., et al. (2021). Self-repair protects microtubules from destruction by molecular motors. Nat. Mater. *20*, 883–891. https://doi.org/10.1038/s41563-020-00905-0.

39. Andreu-Carbo, M., Fernandes, S., Velluz, M.C., Kruse, K., and Aumeier, C. (2022). Motor usage imprints microtubule stability along the shaft. Dev. Cell *57*, 5–18.e18. https://doi.org/10.1016/j.devcel.2021.11.019.

40. Kalinski, A.L., Kar, A.N., Craver, J., Tosolini, A.P., Sleigh, J.N., Lee, S.J., Hawthorne, A., Brito-Vargas, P., Miller-Randolph, S., Passino, R., et al. (2019). Deacetylation of Miro1 by HDAC6 blocks mitochondrial transport and mediates axon growth inhibition. J. Cell Biol. *218*, 1871–1890. https://doi.org/10.1083/jcb.201702187.

41. Zilberman, Y., Ballestrem, C., Carramusa, L., Mazitschek, R., Khochbin, S., and Bershadsky, A. (2009). Regulation of microtubule dynamics by inhibition of the tubulin deacetylase HDAC6. J. Cell Sci. *122*, 3531–3541. https://doi.org/10.1242/jcs.046813.

42. Bartolini, F., Andres-Delgado, L., Qu, X., Nik, S., Ramalingam, N., Kremer, L., Alonso, M.A., and Gundersen, G.G. (2016). An mDia1-INF2 formin activation cascade facilitated by IQGAP1 regulates stable microtubules in migrating cells. Mol. Biol. Cell *27*, 1797–1808. https://doi.org/10.1091/mbc.E15-07-0489.

43. Area-Gomez, E., Del Carmen Lara Castillo, M., Tambini, M.D., Guardia-Laguarta, C., de Groof, A.J.C., Madra, M., Ikenouchi, J., Umeda, M., Bird, T.D., Sturley, S.L., and Schon, E.A. (2012). Upregulated function of mitochondria-associated ER membranes in Alzheimer disease. EMBO J. *31*, 4106–4123. https://doi.org/10.1038/emboj.2012.202.

44. Area-Gomez, E., and Schon, E.A. (2017). On the Pathogenesis of Alzheimer's Disease: The MAM Hypothesis. FASEB J *31*, 864–867. https://doi.org/10.1096/fj.201601309.

45. Montesinos, J., Pera, M., Larrea, D., Guardia-Laguarta, C., Agrawal, R.R., Velasco, K.R., Yun, T.D., Stavrovskaya, I.G., Xu, Y., Koo, S.Y., et al. (2020). The Alzheimer's disease-associated C99 fragment of APP regulates

cellular cholesterol trafficking. EMBO J. *39*, e103791. https://doi.org/10.15252/embj.2019103791.

46. Bienias, K., Fiedorowicz, A., Sadowska, A., Prokopiuk, S., and Car, H. (2016). Regulation of sphingomyelin metabolism. Pharmacol. Rep. *68*, 570–581. https://doi.org/10.1016/j.pharep.2015.12.008.

47. Grimm, M.O.W., Grimm, H.S., Pätzold, A.J., Zinser, E.G., Halonen, R., Duering, M., Tschäpe, J.A., De Strooper, B., Müller, U., Shen, J., and Hartmann, T. (2005). Regulation of cholesterol and sphingomyelin metabolism by amyloid-beta and presenilin. Nat. Cell Biol. *7*, 1118–1123. https://doi.org/10.1038/ncb1313.

48. Barbullushi, K., Abati, E., Rizzo, F., Bresolin, N., Comi, G.P., and Corti, S. (2019). Disease Modeling and Therapeutic Strategies in CMT2A: State of the Art. Mol. Neurobiol. *56*, 6460–6471. https://doi.org/10.1007/s12035-019-1533-2.

49. El Fissi, N., Rojo, M., Aouane, A., Karatas, E., Poliacikova, G., David, C., Royet, J., and Rival, T. (2018). Mitofusin gain and loss of function drive pathogenesis in Drosophila models of CMT2A neuropathy. EMBO Rep. *19*, e45241. https://doi.org/10.15252/embr.201745241.

50. Zuchner, S., Mersiyanova, I.V., Muglia, M., Bissar-Tadmouri, N., Rochelle, J., Dadali, E.L., Zappia, M., Nelis, E., Patitucci, A., Senderek, J., et al. (2004). Mutations in the mitochondrial GTPase mitofusin 2 cause Charcot-Marie-Tooth neuropathy type 2A. Nat. Genet. *36*, 449–451. https://doi.org/10.1038/ng1341.

51. Chung, K.W., Kim, S.B., Park, K.D., Choi, K.G., Lee, J.H., Eun, H.W., Suh, J.S., Hwang, J.H., Kim, W.K., Seo, B.C., et al. (2006). Early onset severe and late-onset mild Charcot-Marie-Tooth disease with mitofusin 2 (MFN2) mutations. Brain *129*, 2103–2118. https://doi.org/10.1093/brain/awl174.

52. Zuchner, S., De Jonghe, P., Jordanova, A., Claeys, K.G., Guergueltcheva, V., Cherninkova, S., Hamilton, S.R., Van Stavern, G., Krajewski, K.M., Stajich, J., et al. (2006). Axonal neuropathy with optic atrophy is caused by mutations in mitofusin 2. Ann. Neurol. *59*, 276–281. https://doi.org/10.1002/ana.20797.

53. Nemoto, Y., and De Camilli, P. (1999). Recruitment of an alternatively spliced form of synaptojanin 2 to mitochondria by the interaction with the PDZ domain of a mitochondrial outer membrane protein. EMBO J. *18*, 2991–3006.

54. Detmer, S.A., and Chan, D.C. (2007). Complementation between mouse Mfn1 and Mfn2 protects mitochondrial fusion defects caused by CMT2A disease mutations. J. Cell Biol. *176*, 405–414. https://doi.org/10.1083/jcb.200611080.

55. Howes, S.C., Alushin, G.M., Shida, T., Nachury, M.V., and Nogales, E. (2014). Effects of tubulin acetylation and tubulin acetyltransferase binding on microtubule structure. Mol. Biol. Cell *25*, 257–266. https://doi.org/10.1091/mbc.E13-07-0387.

56. Coombes, C., Yamamoto, A., McClellan, M., Reid, T.A., Plooster, M., Luxton, G.W.G., Alper, J., Howard, J., and Gardner, M.K. (2016). Mechanism of microtubule lumen entry for the alpha-tubulin acetyltransferase enzyme alphaTAT1. Proc. Natl. Acad. Sci. USA *113*, E7176–E7184. https://doi.org/10.1073/pnas.1605397113.

57. Even, A., Morelli, G., Broix, L., Scaramuzzino, C., Turchetto, S., Gladwyn-Ng, I., Le Bail, R., Shilian, M., Freeman, S., Magiera, M.M., et al. (2019). ATAT1-enriched vesicles promote microtubule acetylation via axonal transport. Sci. Adv. *5*, eaax2705. https://doi.org/10.1126/sciadv.aax2705.

58. Ly, N., Elkhatib, N., Bresteau, E., Piétrement, O., Khaled, M., Magiera, M.M., Janke, C., Le Cam, E., Rutenberg, A.D., and Montagnac, G. (2016). alphaTAT1 controls longitudinal spreading of acetylation marks from open microtubules extremities. Sci. Rep. *6*, 35624. https://doi.org/10.1038/srep35624.

59. Montagnac, G., Meas-Yedid, V., Irondelle, M., Castro-Castro, A., Franco, M., Shida, T., Nachury, M.V., Benmerah, A., Olivo-Marin, J.C., and Chavrier, P. (2013). alphaTAT1 catalyses microtubule acetylation at clathrin-coated pits. Nature *502*, 567–570. https://doi.org/10.1038/nature12571.

60. Devine, M.J., Birsa, N., and Kittler, J.T. (2016). Miro sculpts mitochondrial dynamics in neuronal health and disease. Neurobiol. Dis. *90*, 27–34. https://doi.org/10.1016/j.nbd.2015.12.008.

61. Davis, K., Basu, H., Izquierdo-Villalba, I., Shurberg, E., and Schwarz, T.L. (2023). Miro GTPase domains regulate the assembly of the mitochondrial motor-adaptor complex. Life Sci. Alliance *6*, e202201406. https://doi.org/10.26508/lsa.202201406.

62. Eshun-Wilson, L., Zhang, R., Portran, D., Nachury, M.V., Toso, D.B., Löhr, T., Vendruscolo, M., Bonomi, M., Fraser, J.S., and Nogales, E. (2019). Effects of alpha-tubulin acetylation on microtubule structure and stability. Proc. Natl. Acad. Sci. USA *116*, 10366–10371. https://doi.org/10.1073/pnas.1900441116.

63. Nunes, M.J., Moutinho, M., Gama, M.J., Rodrigues, C.M.P., and Rodrigues, E. (2013). Histone deacetylase inhibition decreases cholesterol levels in neuronal cells by modulating key genes in cholesterol synthesis, uptake and efflux. PLoS One *8*, e53394. https://doi.org/10.1371/journal.pone.0053394.

64. Park, H.J., Kim, H.J., Hong, Y.B., Nam, S.H., Chung, K.W., and Choi, B.O. (2014). A novel INF2 mutation in a Korean family with autosomal dominant intermediate Charcot-Marie-Tooth disease and focal segmental glomerulosclerosis. J. Peripher. Nerv. Syst. *19*, 175–179. https://doi.org/10.1111/jns5.12062.

65. Castro-Castro, A., Janke, C., Montagnac, G., Paul-Gilloteaux, P., and Chavrier, P. (2012). ATAT1/MEC-17 acetyltransferase and HDAC6 deacetylase control a balance of acetylation of alpha-tubulin and cortactin and regulate MT1-MMP trafficking and breast tumor cell invasion. Eur. J. Cell Biol. *91*, 950–960. https://doi.org/10.1016/j.ejcb.2012.07.001.

66. Davenport, A.M., Collins, L.N., Chiu, H., Minor, P.J., Sternberg, P.W., and Hoelz, A. (2014). Structural and functional characterization of the alpha-tubulin acetyltransferase MEC-17. J. Mol. Biol. *426*, 2605–2616. https://doi.org/10.1016/j.jmb.2014.05.009.

67. Pero, M.E., Meregalli, C., Qu, X., Shin, G.J.E., Kumar, A., Shorey, M., Rolls, M.M., Tanji, K., Brannagan, T.H., Alberti, P., et al. (2021). Pathogenic role of delta 2 tubulin in bortezomib-induced peripheral neuropathy. P Natl Acad Sci USA *118*. ARTN e2012685118. https://doi.org/10.1073/pnas.2012685118.

68. Qu, X., Kumar, A., Blockus, H., Waites, C., and Bartolini, F. (2019). Activity-Dependent Nucleation of Dynamic Microtubules at Presynaptic Boutons Controls Neurotransmission. Curr. Biol. *29*, 4231–4240.e5. https://doi.org/10.1016/j.cub.2019.10.049.

69. Chen, H., Detmer, S.A., Ewald, A.J., Griffin, E.E., Fraser, S.E., and Chan, D.C. (2003). Mitofusins Mfn1 and Mfn2 coordinately regulate mitochondrial fusion and are essential for embryonic development. J. Cell Biol. *160*, 189–200. https://doi.org/10.1083/jcb.200211046.

70. Khawaja, S., Gundersen, G.G., and Bulinski, J.C. (1988). Enhanced stability of microtubules enriched in detyrosinated tubulin is not a direct function of detyrosination level. J. Cell Biol. *106*, 141–149. https://doi.org/10.1083/jcb.106.1.141.

71. Bligh, E.G., and Dyer, W.J. (1959). A rapid method of total lipid extraction and purification. Can. J. Biochem. Physiol. *37*, 911–917. https://doi.org/10.1139/o59-099.

72. Vance, J.E. (2008). Phosphatidylserine and phosphatidylethanolamine in mammalian cells: two metabolically related aminophospholipids. J. Lipid Res. *49*, 1377–1387. https://doi.org/10.1194/jlr.R700020-JLR200.

73. Shin, G.J.E., Pero, M.E., Hammond, L.A., Burgos, A., Kumar, A., Galindo, S.E., Lucas, T., Bartolini, F., and Grueber, W.B. (2021). Integrins protect sensory neurons in models of paclitaxel-induced peripheral sensory neuropathy. Proc. Natl. Acad. Sci. USA *118*, e2006050118. https://doi.org/10.1073/pnas.2006050118.

STAR★METHODS

KEY RESOURCES TABLE

REAGENT or RESOURCE	SOURCE	IDENTIFIER
Antibodies		
Mouse monoclonal mitofusin-2 (6A8)	Abcam	Cat# ab56889; RRID:AB_2142629
Rabbit monoclonal mitofusin-2	Abcam	Cat# ab124773; RRID:AB_10999860
Mouse monoclonal mitofusin-2	Proteintech	Cat# 67487-1-Ig; RRID:AB_2882713
Rabbit polyclonal IQGAP1	Novus Biologicals	Cat# NBP1-06529; RRID:AB_1582398)
Rabbit polyclonal HDAC6	Novus Biologicals	Cat# NBP1-78981; RRID:AB_11037211
Rabbit polyclonal ATAT1	Bioss	Cat#Bs-9535R
Rabbit polyclonal ATAT1 (C6orf134) (For Figures 3 and S7 IF)	Proteintech	Cat# 28828-1-AP; RRID:AB_2881219
Rabbit monoclonal TOMM20	Abcam	Cat# ab186735; RRID:AB_2889972
Mouse monoclonal TOMM20	Millipore Sigma	Cat#KB061-4F3
Rabbit polyclonal detyrosinated tubulin	Abcam	Cat#ab48389; RRID:AB_869990
Rat tyrosinated tubulin, clone YL1/2	Millipore	Cat# MAB1864; RRID:AB_2210391
Mouse monoclonal acetylated tubulin	Sigma Aldrich	Cat# T6793; RRID:AB_477585
Mouse monoclonal DM1A	Sigma Aldrich	Cat# T6199; RRID:AB_477583
Human anti-tubulin GTP (MB11)	Adipogen	Cat# AG-27B-0009; RRID:AB_2490499
Rabbit polyclonal TTL	Proteintech	Cat# 13618-1-AP; RRID:AB_2256858
Mouse monoclonal PDI	Santacruz	Cat# sc-74551; RRID:AB_2156462
Mouse monoclonal anti-c-Myc 9E10 HRP	Santacruz	Cat#SC-40 HRP
Mouse monoclonal anti-c-Myc 9E10 Agarose	Santacruz	Cat# sc-40 AC; RRID:AB_2857941
Mouse monoclonal anti-Flag M2 HRP	Sigma Aldrich	Cat# A8592; RRID:AB_439702
Mouse monoclonal anti-Flag M2 Agarose	Sigma Aldrich	Cat# A2220, RRID:AB_10063035
Chicken polyclonal neurofilament	Aves labs	Cat# AB_2313553 NFL; RRID:AB_2313553
Mouse monoclonal Miro-1(CL1083)	Abcam	Cat#Ab188029
Rabbit polyclonal acetyl-Miro1 (Lys105)	Millipore	Cat#ABS2247
Rabbit polyclonal anti-Miro2	Proteintech	Cat#11235-1-AP
Rabbit polyclonal anti-Kif5c	Proteintech	Cat# 25897-1-AP; RRID:AB_2880288
Mouse monoclonal Cox4	ThermoFisher	Cat# MA5-15078; RRID:AB_10987478
Mouse monoclonal GAPDH	Abcam	Cat# ab8245; RRID:AB_2107448
Rabbit polyclonal GAPDH	ThermoFisher	Cat# PA1-987; RRID:AB_2107311
Goat anti-mouse IgG (H+L) highly cross-adsorbed secondary antibody, Alexa Flour 488-conjugated	ThermoFisher	Cat#A11029
Goat anti-rabbit IgG (H+L) highly cross-adsorbed secondary antibody, Alexa Flour 488-conjugated	ThermoFisher	Cat# A-11034; RRID:AB_2576217
Goat anti-mouse IgG (H+L) highly cross-adsorbed secondary antibody, Alexa Flour 546-conjugated	ThermoFisher	Cat# A-11030; RRID:AB_2737024
Goat anti-rabbit IgG (H+L) highly cross-adsorbed secondary antibody, Alexa Flour 546-conjugated	ThermoFisher	Cat# A-11035; RRID:AB_2534093
Goat anti-human IgG (H+L) highly cross-adsorbed secondary antibody, Alexa Flour 568-conjugated	ThermoFisher	Cat# A-21090; RRID:AB_2535746
IRDye® 680RD Goat anti-mouse IgG secondary antibody	LI-COR	Cat# 926-68070; RRID:AB_10956588
IRDye® 800CW Goat anti-rabbit IgG secondary antibody	LI-COR	Cat# 926-32211; RRID:AB_621843

Continued

REAGENT or RESOURCE	SOURCE	IDENTIFIER
IRDye® 680RD Goat anti-rabbit IgG secondary antibody	LI-COR	Cat# 926-68071; RRID:AB_10956166
IRDye® 800CW Goat anti-rabbit IgG secondary antibody	LI-COR	Cat# 926-32211; RRID:AB_621843
Bacterial strains		
DH5 alpha	New England Biolabs	Cat#C2987I
XL1-Blue	Agilent	Cat#200229
Chemicals, peptides and recombinant proteins		
Trichostatin A (TSA)	Tocris	Cat#1406
Tubacin	Millipore Sigma	Cat#SML0065
Mitotracker Red CMXROS	Thermofisher	Cat#M7512
DMEM	Gibco	Cat#11995-065
Neurobasal	Thermofisher	Cat#110349
Fetal bovine serum	HyClone	Cat#SH30071.03
Bovine calf serum	Thermofisher	Cat#26170043
B-27 supplement (50x)	Thermofisher	Cat#7504044
Penicillin-streptomycin	Thermofisher	Cat#15140163
10x HBSS	Thermofisher	Cat#14065056
Cytosine β-D-arabinofuranoside hydrochloride (AraC)	Millipore Sigma	Cat#C6645
Collagenase	Millipore Sigma	Cat#C0130
Trypsin 0.05% EDTA	Thermofisher	Cat#25300054
GlutaMAX Supplement	Thermofisher	Cat#35050061
Poly-D-Lysine	Sigma Aldrich	Cat#P1149
Laminin	Sigma Aldrich	Cat#11243217001
Laemlli SDS sample buffer, reducing	Thermofisher	Cat#J60015-AD
NuPAGE MOPS SDS Running buffer	Thermofisher	Cat#NP0001
Fluoromount-G	Southern Biotech	Cat#0100-01
32% PFA	EMS	Cat#15714-S
DreamFect™Gold transfection reagent	OZ Bioscience	Cat#DG80500
c-Myc Peptide	Sigma Aldrich	Cat#M2435
Flag peptide	Sigma Aldrich	Cat#F3290
Critical commercial assays		
DuoLink PLA *In Situ* Red starter mouse/rabbit kit	Sigma-Aldrich	DUO92101
Experimental models: Organisms/strains		
UAS-MARF RNAi	Bloomington Stock Center	BL 31157
UAS-MARF miRNA CDS	Bloomington Stock Center	BL 67158
Mouse: C57BL/6J	Charles River Laboratories	RRID:IMSR_CRL:027
Recombinant DNA		
pLKO.1 shMfn2	Sigma Aldrich	TRCN0000080608
pLKO.1 shTTL	Sigma Aldrich	TRCN0000191515
MFN2 7X Myc in pCLBW	Detmer and Chan[54]	NA
MFN2 R94W 7X Myc in pCLBW	Detmer and Chan[54]	NA
MFN2 T105M 7X Myc in pCLBW	Detmer and Chan[54]	NA
Flag-ATAT1 WT	Laurent Ngyuen	NA
Flag-ATAT1 (1-242)	Laurent Ngyuen	NA
Flag-ATAT1 (1-286)	Laurent Ngyuen	NA

Continued

REAGENT or RESOURCE	SOURCE	IDENTIFIER
Zsgreen-MFN1	Estella Area Gomez	NA
Mito-dendra2	Addgene	55796
pLV OMP25 (rtOMP25; NM 022599.2; Promoter: SYN1; Linker: IRES; Fluorescent tag: EmGFP)	VectorBuilder; This paper supplementary	VB220328-1304ynx
pLV hATAT1-OMP25 [hATAT1 (isoform#2, NM_024904.5) rtOMP25 C-terminal; Promoter: SYN1; Linker: IRES; Fluorescent tag: EmGFP]	VectorBuilder; This paper supplementary	VB220329-1381pbx
Software		
ImageJ (Fiji)	NIH	RRID:SCR_002285
GraphPad Prism	GraphPad	RRID:SCR_002798
Li-COR Image Studio Software	Li-COR	RRID:SCR_015795
Zeiss ZEN	Zeiss	RRID:SCR_013672
Andor iQ3	Oxford Instruments	RRID:SCR_014461
Other		
18 mm No.1 circle coverglass	Carolina	633033
35 mm MatTek dishes	MatTek	P35G-1.5-14-C
NuPAGE Gel	ThermoFisher	NP0316
Nitrocellulose membrane	Fisher	10600011

RESOURCE AVAILABILITY

Lead contact

Francesca Bartolini (fb2131@columbia.edu).

Materials availability

Further information and requests for resources and unique reagents should be directed to and will be fulfilled by the lead contact, Francesca Bartolini (fb2131@columbia.edu).

Data and code availability

- All datasets reported in this work are available from the lead contact upon request.
- This paper does not report original code.
- Any additional information required in this paper is available from the lead contact upon request.

EXPERIMENTAL MODEL AND STUDY PARTICIPANT DETAILS

Mice for primary cell cultures

All protocols and procedures for mice were approved by the Committee on the Ethics of Animal Experiments of Columbia University and according to Guide for the Care and Use of Laboratory Animals of the National Institutes of Health. All experiments with mice to generate adult DRG cultures were sex balanced and no influence of gender was observed.

Drosophila melanogaster

All animals were randomly selected regardless of sex.

Cell lines

WT, Mfn2 KO, Mfn1 KO (kind gifts of Dr. Area-Gomez) and Iqgap1 KO mouse embryonic fibroblast cells were grown in DMEM supplemented with 10% fetal bovine serum. Cells were grown to 80% confluency on acid treated glass coverslips prior to experiment. Cells were transfected using DreamFect Gold transfection reagent according to manufacturer's protocol. 1-2 ug of DNA were diluted in low serum DMEM medium and 2-4 ul of DreamFect Gold transfection reagent. Solution was incubated for 20 min at R.T. and added in cells and incubated overnight at 37°C. All cell lines have been authenticated through western blot analysis using specific antibodies and all the experiments were conducted using mycoplasma-free cells, which was monitored using PCR methods.

METHOD DETAILS

Confocal microscopy and analysis

Cells were fixed in 4% PFA for 15 min and permeabilized with 0.1% Triton X-100 for 5 min at R.T. For the MT cytoskeleton, cells were fixed in ice cold MetOH for 10' prior to rehydration in PBS buffer. Cells were then washed in PBS, blocked in 2% FBS and 2% BSA in PBS for 1 h, stained with primary antibodies overnight at 4°C followed by secondary antibodies for 1 h. Mounted samples were observed using a Zeiss LSM 800 confocal microscope using a 63x objective (Plan-Apochromat, NA 1.4). Z stack (0.5 um) images were acquired. To calculate the Mitotic Index as percentage, the number of cells in mitosis were divided by the total number of cells multiplied by 100. To calculate ratio of acetylated/tyrosinated tubulin intensity, each file was converted to 8-bit greyscale and maximum projection images were generated by using Image J. ROIs were selected in both channels to calculate mean fluorescence and integrated density prior to calculating corrected total fluorescence intensity (CTCF= Integrated Density – (Area of selected cell * Mean fluorescence of background readings). For measuring MT associated MB11 intensity, an ROI was selected along individual tyrosinated MTs using ImageJ and GTP tubulin (hMB11) pixel intensity was calculated along the tyrosinated tubulin signal and corrected by subtracting out background signal fluorescence intensity.

Airyscan confocal microscopy and analysis

For immunofluorescence staining of the MT cytoskeleton, cells were fixed in ice cold MetOH for 10' prior to rehydration in PBS buffer. For all other stainings, cells were fixed in 4% PFA for 15 min and permeabilized with 0.1% Triton X-100 for 5 min at R.T. Cells were then washed in PBS, blocked in 2% FBS and 2% BSA in PBS for 1 h, stained with primary antibodies overnight at 4°C followed by secondary antibodies for 1 h. Mounted samples were observed using a Zeiss LSM 800 confocal microscope equipped with Airyscan module, using a 63x objective (Plan-Apochromat, NA 1.4). Z stack (0.2 um) images were acquired and processed using Zen Blue 2.1 software prior to analysis by ImageJ software. For 3D reconstruction, mitochondrial networks in individual cells were quantified by analyzing the network volume using Imaris software (Bitplane, Concord, MA). For line scan analysis, a line was drawn, and intensity was measured represented as gray values. The amount of fluorescence of the colocalizing pixels in each channel (Mander's coefficient) was calculated using ImageJ. The file was opened, and channels were split. Each select file was changed to 8-bit greyscale and max projection images was generated. We assessed colocalization by Plugin co-localization finder. To calculate number of ATAT1 foci, each image was converted into an 8-bit greyscale image and ATAT1 signal thresholded until the foci appeared isolated from the background in a binary image. Both channels were then merged into one and the number of foci localizing in the merged stack quantified. To calculate ATAT1 localization with MFN2 on mitochondria, numbers of ATAT1 and MFN2 foci were quantified on each channel individually. Both channels were then merged into one and number of foci in the merged stack analyzed and quantified on mitochondria.

Western blot analysis

Cells were lysed in Laemmli sample buffer and boiled at 96°C for 5 min. Cell lysates were sonicated with a probe sonicator to sheer cellular debris and genomic DNA. Proteins were separated by 10% Bis-Tris gel (Invitrogen) and transferred onto nitrocellulose membrane. After blocking in 5% milk/TBS or BSA/TBS, membranes were incubated with primary antibodies at 4°C overnight prior to 1 h incubation with secondary antibodies. Image acquisition was performed with an Odyssey imaging system (LI-COR Biosciences, NE) and analyzed with Odyssey software.

Proximity ligation assay (PLA)

PLA assays were carried out using a Duolink *in situ* red starter kit mouse/rabbit kit (Sigma-Aldrich) according to the manufacturer's protocol. The primary antibodies used were mouse anti-MFN2 (1:100 dilution), anti-ATAT1 (1:50 dilution), anti-Miro1 (1:50 dilution). Z stack images were acquired on a Zeiss LSM 800 confocal microscope using a 63x objective (Plan-Apochromat, NA 1.4) and puncta were analyzed using ImageJ/FIJI. Each image was processed and the channel containing the PLA signal was thresholded until the PLA puncta were reliably isolated from the background forming a binary image. Overlapping PLA puncta were segmented using a watershed function. Size thresholding was adjusted, and the number of PLA puncta were then counted in each cell.

Analysis of mitochondrial morphology, motility and distribution

Mitochondria were labeled using mitoTracker Red CMROX according to manufacturer protocol (Thermo Fisher Scientific) and detected by epifluorescence microscope equipped with 60 x objective lens (Olympus IX81) and a monochrome CCD camera (Sensicam QE, Cooke Corporation). Aspect ratio (length/width) were measured in unedited image files by using Image J/FIJI. Brightness and contrast of the images were adjusted to optimize visualization of the mitochondrial segments and to reduce background noise. After selecting an individual cell, the Analyze Particles function (pixel size 10-infinitiy; circularity 0.00–1.00) was used to count the number of noncontiguous, discrete particles, and describe their shape. For mitochondrial distribution and displacement velocity mitochondria were live imaged for 3 min at 2 sec/frame at 37°C. A customized Mitoplot software (kind gift of Dr. Gregg Gundersen) was used for analyzing mitochondrial distribution by defining the center of cell and drawing a line towards periphery. Manual tracking plug-in in ImageJ/FIJI was used to analyze mitochondrial displacement velocity by selecting individual mitochondria.

Microtubule dynamics

Fibroblasts were transfected with pMSCV-puro-tagGFP-C4 α-tubulin plasmid to generate a green fluorescent protein (GFP)–tubulin stably expressing cell line. Live imaging of MT dynamics in transfected cells was performed at 37°C and 5% CO_2 for 5 min (5 s/f) with a 100× PlanApo objective (numerical aperture 1.45) and an iXon X3 CCD camera (Andor, Belfast, United Kingdom) on a Nikon Eclipse Ti microscope controlled by Nikon's NIS-Elements software (Nikon, Tokyo, Japan). Movies were analyzed by ImageJ using a manual tracking plug-in. Dynamicity is calculated by dividing the sum of growth and shrinkage distances by MT lifetime.

Mitodendra

Dendra2 photoconversion and imaging utilized the protocol from Evrogen. Images were acquired with an Olympus spinning disk microscope EC-Plan-Neofluar 40X/1.3 oil. Z-stack acquisitions over-sampled each optical slice twice, and the Zen 2009 image analysis software was used for maximum z-projections. The 488 nm laser line and the 561 nm laser excited Dendra2 in the unconverted state and photo-converted state, respectively. To photo-switch Dendra2, a region was illuminated with the 405 nm line (4% laser power) for 90 bleaching iterations. The corrected total fluorescence intensity of both the channels was calculated using ImageJ and colocalization percentage was calculated.

Lentivirus production

Production of lentiviral particles was conducted using the second-generation packaging system.[67,68] In brief, HEK293T cells were co-transfected with lentiviral plasmid shRNA and the packaging vectors pLP1, pLP2, and pLP-VSV-G (Thermo Fisher) using the Ca^{2+} phosphate transfection method. At 24, 36, and 48 h after transfection, the virus-containing supernatant was collected, and the lentiviral particles concentrated (800-fold) by ultracentrifugation (100,000 × g at 4°C for 2 h) prior to aliquoting and storage at −80°C.

Retrovirus production

MFN2 Myc, MFN2 R94W Myc and MFN2 T105M Myc cDNAs were cloned into the retroviral construct pCLBW[69] and the retroviral particles generated as detailed in.[54,69] Briefly, retroviral expression vectors were cotransfected with the ecotropic retroviral packaging vector pCLEco into 293T cells. 48 h after transfection retroviral particles were harvested by pelleting cells and debris at 900 × g for 5 min. Supernatants were passed through 0.45 μm syringe filters, aliquoted and immediately frozen on dry ice prior to storing at -80°C.

MT stability

WT and Mfn2 KO MEFs were incubated at 8°C for 30 min to induce mild MT depolymerization. At the end of the incubation time, cells were gently washed with PEM 1× buffer (85 mM Pipes, pH 6.94, 10 mM EGTA, and 1 mM $MgCl_2$) twice before extraction with PEM buffer, supplemented with 0.05 % Triton X-100. After 1 min extraction at 8°C, a matching volume of fixative buffer (ice cold MetOH) was added dropwise to the coverslips, and cells were incubated for another 5 min at -20°C. Cells were finally washed with 1x PBS and processed for immunofluorescence labeling. Mounted samples were observed using a Zeiss LSM 800 confocal microscope using a 63x objective (Plan-Apochromat, NA 1.4). Z stack (0.5 um) images were acquired and processed using Zen Blue 2.1 software. All images were analyzed using ImageJ software as published.[70] Each select file was changed to 8-bit greyscale and max projection images were generated. Using Image J area was selected in to calculate corrected total fluorescence intensity for DM1A tubulin after extraction and normalized to total DM1A tubulin intensity.

Analysis of phospholipid synthesis in cultured cells

Both mitochondria and ER play key roles in the synthesis of phosphatidylserine (PtdSer), phosphatidylethanolamine (PtdEtn), and phosphatidylcholine (PtdCho). PtdSer is synthesized in the MAM; it then translocates to mitochondria, where it is converted to PtdEtn; PtdEtn then translocates back to the MAM, to generate PtdCho.[71] To test the effect of MFN2 on phospholipid synthesis mediated by MAM, WT and Mfn2 KO MEF cells were incubated for 2 h with serum-free medium to ensure removal of exogenous lipids. The medium was then replaced with MEM containing 2.5 μCi/ml of ^{3}H-serine for 2, 4 and 6 h. The cells were washed and collected in DPBS, pelleted at 2500 g for 5 min at 4°C, and resuspended in 0.5 ml water, removing a small aliquot for protein quantification. Lipid extraction was done by the Bligh and Dyer method. Briefly, three volumes of chloroform/methanol 2:1 were added to the samples and vortexed. After centrifugation at 8000 g for 5 min, the organic phase was washed twice with two volumes of methanol/water 1:1, and the organic phase was blown to dryness under nitrogen. Dried lipids were resuspended in 60 μl of chloroform/methanol 2:1 (v/v) and applied to a TLC plate. Phospholipids were separated using two solvents, composed of petroleum ether/diethyl ether/acetic acid 84:15:1 (v/v/v) and chloroform/methanol/acetic acid/water 60:50:1:4 (v/v/v/v). Development was performed by exposure of the plate to iodine vapor. The spots corresponding to the relevant phospholipids (identified using co-migrating standards) were scraped and counted in a scintillation counter (Packard Tri-Carb 2900TR). Both mitochondria and ER play key roles in the synthesis of phosphatidylserine (PtdSer), phosphatidylethanolamine (PtdEtn), and phosphatidylcholine (PtdCho). PtdSer is synthesized in the MAM; it then translocates to mitochondria, where it is converted to PtdEtn; PtdEtn then translocates back to the MAM, to generate PtdCho.[72] Therefore, to directly test the effect of MFN2 mutations on phospholipid synthesis mediated by MAM, we incubated control and Mfn2 KO fibroblasts in medium containing ^{3}H-serine and measured the incorporation of the label into newly synthesized ^{3}H-PtdSer and ^{3}H-PtdEtn after 2 and 4 h.

Lipidomics

All samples were collected and treated following recently accepted guidelines for the analysis of human blood plasma and/or serum. Lipids were extracted from equal amounts of material (0.2 ml/sample) by a chloroform–methanol extraction method. Three comprehensive panels, scanning for either positive lipids, negative lipids or neutral lipids (under positive mode), were analyzed. Equal amounts of internal standards with known concentrations were spiked into each extract. Each standard was later used to calculate the concentrations of corresponding lipid classes by first calculating ratio between measured intensities of a lipid species and that of corresponding internal standard multiplied by the known concentration of the internal standard. Samples were analyzed using a 6490 Triple Quadrupole LC/MS system (Agilent Technologies, Santa Clara, CA). Cholesterol and cholesterol esters were separated with normal-phase HPLC using an Agilent Zorbax Rx-Sil column (inner diameter 2.1 Å$\sim$ 100 mm) under the following conditions: mobile phase A (chloroform:methanol:1 M ammonium hydroxide, 89.9:10:0.1, v/v/v) and mobile phase B (chloroform:methanol:water: ammonium hydroxide, 55:39.9:5:0.1, v/v/v/v); 95% A for 2 min, linear gradient to 30% A over 18 min and held for 3 min, and linear gradient to 95% A over 2 min and held for 6 min.

Cellular fractionation

WT and Mfn2 KO fibroblasts were cultured on 15 cm petri dishes. Buffer A (10 mM HEPES, 1.5 mM MgCl$_2$, 10 mM KCl, 0.5 mM DTT, 0.05% NP40, pH 7.9) was prepared freshly and protease and phosphatase inhibitors were added. Cells were scraped thoroughly using 1 ml of buffer A and left on ice for 10 min. Samples were centrifuged at 3000 rpm on a table top centrifuge for 10 min at 4°C and supernatants were stored on ice. Pellets were resuspended in buffer B (5 mM HEPES, 1.5 mM MgCl$_2$, 0.2 mM EDTA, 0.5 mM DTT, 26% Glycerol (v/v), pH 7.9) and 1 ul of 4.6 M NaCl was added to a final concentration of 4.6 mM. Cells were homogenized with 20 full strokes of Dounce homogenizer on ice and left on ice for 30 min. Samples were centrifuged at 3000 rpm for 10 min at 4°C. Pellet contains the nuclear fraction and supernatant contains the cytosolic fraction. For the mitochondrial fraction assay, a mitochondrial isolation kit was used (Thermo Scientific, 89874). WT and Mfn2 KO fibroblasts were cultured on 10 cm petri dishes. Cells were pelleted by centrifuging the cell suspension. Protease inhibitors were added to reagent A and C immediately before use. 800 μl of mitochondrial isolation reagent A was added, cells vortexed at medium speed for 5 s and incubated on ice for exactly 2 min. 10 μl of mitochondrial isolation reagent B was added, before vortexing at maximum speed for 5 s and incubating on ice for 5 min with vortexing at every min. 800 μl of Mitochondrial reagent C was added and tubes were inverted several times to mix. Tubes were centrifuged at 700 x g for 10 min at 4°C and supernatants transferred and centrifuged at 12,000 x g for 15 min at 4°C and 3,000 x g for 15 min. Pellets contain the mitochondria fraction. All the samples were processed for western blot analysis.

Isolation of adult DRG neurons

DRG were dissected from 8- to 10-wk-old C57BL/6J mice in cold Hank's balanced salt solution (HBSS) (Life Technologies) or Dulbecco's Modified Eagle's medium (Life Technologies) and dissociated in 1 mg/mL collagenase A for 1 h at 37°C, followed by 0.05% trypsin (Life Technologies) digestion for 3 to 5 min at 37°C and washed with Neurobasal medium (Invitrogen) supplemented with 2% B-27 (Invitrogen), 0.5 mM glutamine (Invitrogen), fetal bovine serum (FBS), and 100 U/mL penicillin-streptomycin. DRG neurons were then triturated by repeated gentle pipetting until no clump was visible, and neuronal bodies were resuspended in Neurobasal medium with FBS prior to plating onto 12 well plates (over 18 mm coverslips) that had been coated overnight with 100 μg/mL poly-D-lysine at 37°C and for 1 h at 37°C with 10 μg/mL laminin (Life Technologies). After 30 min, Neurobasal medium, without FBS, was added to the plate. At 4DIV, at least 30% of media was changed and 10 μM AraC was added to media every 4 d. DRG neurons were treated with lentiviral particles at 7DIV. For overexpression of OMP25 and ATAT1 OMP25 lentiviral particles DRG neurons were infected at 7DIV for 5 days. Myc MFN2 R94W and Myc MFN2 T105M retroviruses were infected at 7 DIV for 5 days in DRG neurons.

Degeneration index in DRG neurons

As reported previously,[67] images of random fields of dissociated adult DRG neurons fixed with 4%PFA and immunostained with mouse anti-neurofilament antibody were acquired using a 20× objective lens (Olympus IX81) coupled to a monochrome CCD camera (Sensicam QE; Cooke Corporation). To quantify axonal degeneration, the areas occupied by the axons (total axonal area) and degenerating axons (fragmented axonal area) were measured in the same field from images of DRG neurons. Images were automatically thresholded (global threshold) using a default auto threshold method, binarized, and the fragmented axonal area measured by using the particle analyzer module of ImageJ (size of small fragments = 20 to 10,000 pixels). Degeneration index was calculated as the ratio between the fragmented axonal area and the total axonal area.

Immunolabeling of *Drosophila* larvae

Immunolabeling of *Drosophila* larvae was performed as in.[73] Briefly, late third instar larvae were dissected in 1 × PBS, fixed in 4% paraformaldehyde (PFA, Electron Microscopy Sciences) in 1 × PBS for 15 min, washed three times in 1 × PBS + 0.3% Triton X-100 (PBS-TX), and blocked for 1 h at R.T. or overnight at 4°C in 5% normal donkey serum (NDS) in PBS-TX (Jackson Immunoresearch). Primary antibodies were chicken anti-GFP (1:1000; Abcam) and acetylated α-tubulin (1:400; Sigma Aldrich) diluted in 5% NDS in PBS-TX. The tissue was incubated overnight in primary antibodies at 4°C and then washed in PBS-TX for 3 × 15 min at R.T. Species-specific, fluorophore-conjugated secondary antibodies (Jackson ImmunoResearch) were used at 1:1000 in 5% NDS in PBS-TX and incubated overnight 4°C. Tissue was washed in PBS-TX for 3 ×

15 min. Immunolabeled tissue was mounted on poly-L-lysine coated coverslips, dehydrated 5 min each in an ascending ethanol series (30, 50, 70, 95, 2 × 100%), cleared in xylenes (2 × 10 min), and mounted in DPX (Fluka).

Imaging and quantification of *Drosophila* sensory neurons

Images of somatosensory neurons from *Drosophila* larvae were acquired using a Yokogawa CSU-W1 SoRa mounted on a Zeiss Axio Observer using a 60x 1.46 NA Alpha Plan-Apochromat oil objective and a 4x magnification changer. Acquisitions included the cell body, axon, and dendrites of somatosensory neurons. Subsequent image analysis was performed using Fiji. Using the md neurons (109(80)2-Gal4, UAS-CD8-GFP) as reference, sub stacks covering the z-depth of each cell body were cropped and blinded for subsequent analysis. Additionally, 2-3 areas (300 x 300 px) devoid of neurons in the same image were selected to measure background levels of acetylated tubulin in each image and used to normalize the levels in the cell body. To measure acetylated tubulin levels in the cell bodies, cell bodies were selected using the polygon selection tool, and the area outside the cell body was cleared to avoid including acetylated tubulin staining surrounding the cell body in the subsequent quantification. Processed z-stacks of cell bodies were z-projected using average intensity. The mean gray value was measured and normalized against background levels of acetylated tubulin quantified in the same image. Raw images were used for quantification. Represented images shown in Figure 5C were deconvolved using Microvolution (20 iterations).

Co-immunoprecipitation assay

HEK293T cells were cultured in Dulbecco's modified Eagle's medium plus 10% fetal bovine serum (FBS), penicillin–streptomycin (1%) and L-glutamine (1%). Transient transfections were performed using DreamFect™Gold transfection reagent (Oz Biosciences SAS, Marseille, FR) in accordance with the manufacturer's protocols. HEK293T cells were lysed in RIPA buffer (50 mM Tris-HCl at pH 7.6, 150 mM NaCl, 0.5% sodium deoxycholic, 5 mM EDTA, 0.1% SDS, 100 mM NaF, 2 mM NaPPi, 1% NP-40) supplemented with protease and phosphatase inhibitors, then centrifuged at 13,000 rpm for 30 min at 4°C and the resulting supernatants were subjected to Bradford protein assay (Bio-Rad, Hercules, California, USA) for measuring total protein concentration. Immunoprecipitations were performed on 1 mg of whole cell extracts by using anti-c-Myc agarose conjugated or anti-Flag M2 agarose (1–2 μg) beads for 2 h at 4°C with rotation. c-Myc peptide or Flag-peptide (0.1 mg/ml) was used as a control. The immunoprecipitated complexes were then washed 5X with RIPA buffer, resuspended in sample loading buffer, boiled for 5 min, resolved by SDS-PAGE, and then subjected to immunoblot analysis.

QUANTIFICATION AND STATISTICAL ANALYSIS

Data distributions that did not pass the normality tests are shown as medians plus interquartile range, and statistical significance was analyzed by nonparametric unpaired two-tailed Mann–Whitney U test or Kruskal–Wallis with Dunn's multiple comparisons test. Data distributions that passed the normality test are shown as mean±SEM, and statistical significance was analyzed by student's t test and two-way ANOVA with Dunnett's multiple comparison. GraphPad prism was used to plot graph. Description of n (samples) or N (population) values are indicated in each figure legend. All experiments were repeated at least three times unless stated otherwise in each figure legend.